Title

Simple Method for Photopatterning Commercial PDMS Using an Off-the-Shelf Photodeactivated Hydrosilylation Inhibitor

Journal

ACS Applied Polymer Materials, 8(7)

ISSN

2637-6105

Authors

Edmunds, SamuelJ

Mallari, Noel SebastienD

Levy, Marc N

et al.

Publication Date

2026-04-10

DOI

10.1021/acsapm.5c04718

ACS APPLIED POLYMER MATERIALS

pubs.acs.org/acsapm Article

Simple Method for Photopatterning Commercial PDMS Using an Off-the-Shelf Photodeactivated Hydrosilylation Inhibitor

Samuel J. Edmunds, Noel Sebastien D. Mallari, Marc N. Levy, Qinyu Liang, Anum Tahir, Dhivya Pushpa Meganathan, Lisa Tang, Leah Sadr, Jacqueline Lampert, Wade Shipley, Hannah E. Fishman, Rafael A. Montalvo, Tarek Rafeedi, Abdulhameed Abdal, Tse Nga Ng, Jinhye Bae, Andrea R. Tao, Nathan A. Romero, Zeinab Jahed, and Darren J. Lipomi*

Cite This: https://doi.org/10.1021/acsapm.5c04718 Read Online

ACCESS | Metrics & More | Article Recommendations | Supporting Information

ABSTRACT: This paper describes a method of micropatterning commercial silicone elastomers using a photodeactivated hydrosilylation inhibitor. The method uses small doses of 365 nm light and is compatible with common platinum-cured formulations of poly(dimethylsiloxane) (PDMS). The hydrosilylation (cross-linking) inhibitor is a UV-sensitive emulsion composed of $FeCl_3$ and a commercially available poly(ethylene oxide)-*co*-PDMS copolymer. This mixture enables selective solidification of exposed regions while preventing solidification in unexposed areas. This approach facilitates the creation of complex geometries while preserving the mechanical tunability, biocompatibility, and optical transparency of the base silicone. The patterned structures have been successfully used to fabricate high-resolution microfluidic devices and substrates for measuring the contractility of cardiac cells with integrated strain gauges. The process achieves feature sizes as small as 20 μm and is compatible with standard photolithography tools.

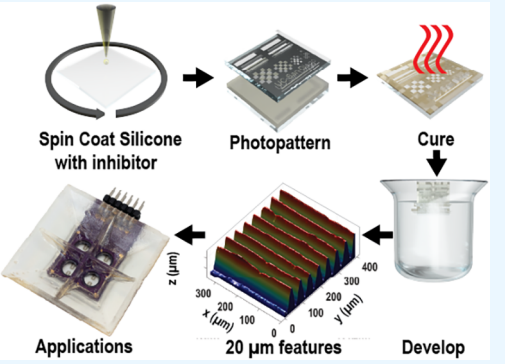

KEYWORDS: *photolithography, PDMS, photochemistry, polymers, microfluidics, BioMEMS, biocompatibility*

1. INTRODUCTION

Silicone elastomers, e.g., poly(dimethylsiloxane) (PDMS), are widely used in scientific and commercial applications due to their high breakdown voltage, optical clarity, tunable mechanical properties, and adjustable surface energies. These properties make them ideal for potting high-voltage circuitry, protective coatings, adhesives, and structural fillers in large 3D constructs such as biomedical implants and prosthetics. In micro- and bioengineering contexts, PDMS is essential for stretchable electronics,[1] wearable microfluidic channels,[2] and soft structures in biological microelectromechanical systems (bioMEMS).[3] These applications frequently require precise, full-thickness patterning of freestanding silicone microstructures with well-defined mechanical properties. Despite the ubiquity of PDMS, there is no simple and broadly accessible method that enables full-thickness, lithographic patterning of commercially available hydrosilylation-based silicone elastomers while preserving their mechanical tunability, optical transparency, and biocompatibility. Existing approaches sacrifice at least one of these constraints (Table S1).

Mechanical patterning methods such as blade cutting, stencil cutting, laser cutting, and embossing (soft lithography)[4] can generate apertures in PDMS films, but suffer from limitations in resolution, alignment accuracy, mechanical integrity, or process scalability.[5−7] Laser cutting, for example, can achieve features near 100 μm,[5] but thermal damage and line-edge roughness are difficult to control.[6] Soft lithography can produce small features, including 20 μm hole arrays,[7] but requires mold fabrication and transfer steps that risk damaging compliant structures and complicate multilayer alignment.

Direct photopatterning of silicone elastomers offers a solution by enabling mask-defined structures and precise multilayer registration. However, most photopatternable formulations described in the literature rely on custom-synthesized precursors or proprietary single-part systems with limited mechanical tunability.[8] In practice, reported systems struggle to simultaneously achieve (i) low exposure dose, (ii) compatibility with commercially available two-part silicones, and (iii) retention of wide mechanical tunability.

Commercial silicone elastomers are predominantly based on three chemistries: radical-initiated curing, platinum-catalyzed

Received: December 18, 2025
Revised: February 21, 2026
Accepted: March 12, 2026

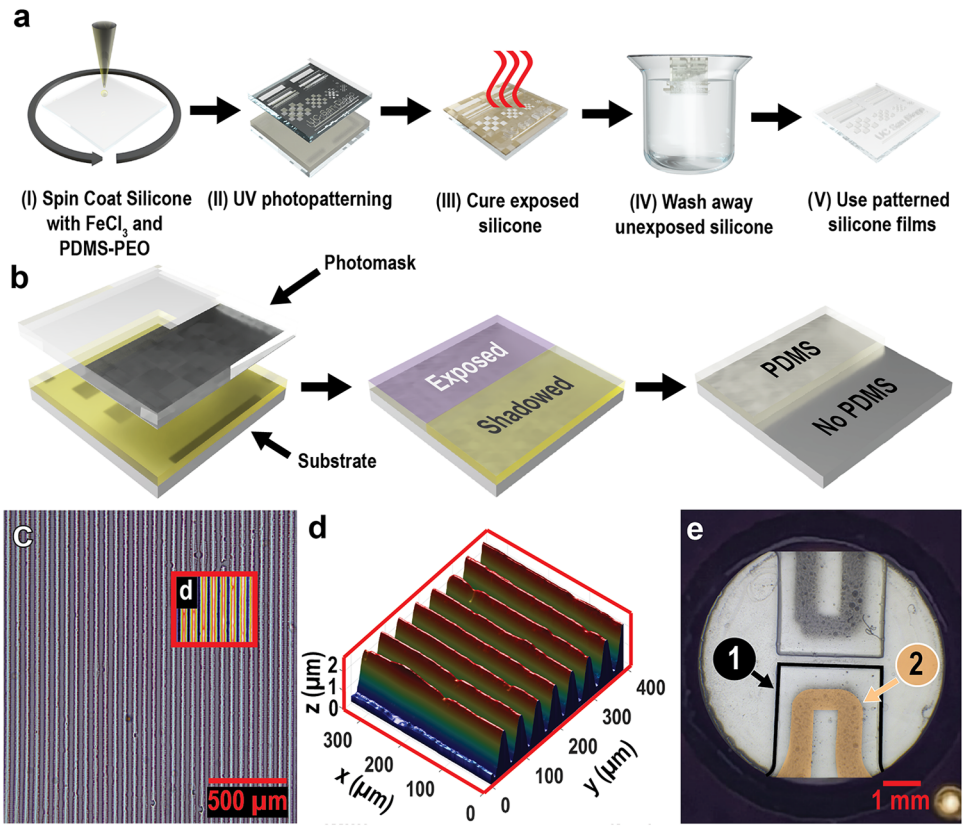

Figure 1. (a) Schematic drawing illustrating the process of patterning silicone elastomers using the photoreactivity of $FeCl_3$ and PEO−PDMS: (I) A film consisting of a liquid silicone prepolymer mixed with the photodeactivated $FeCl_3$ and PEO−PDMS cross-linking inhibitor is spin-coated onto a substrate. (II) The film is exposed to 365 nm UV light through a photomask. (III) The exposed silicone is solidified at 90 °C on a hot plate. (IV) The unexposed silicone is washed away with a solvent such as ethyl acetate. (V) Finished PDMS microstructures. (adapted from ref 28) (b) The addition of $FeCl_3$ and the PEO−PDMS copolymer enables the silicone elastomer to behave like a negative photoresist. (c) Optical microscope image of Sylgard 184 patterned into 20 μm lines spaced 30 μm apart. (d) 3D profile of the Sylgard 184 lines from panel (c). (e) A bioMEMS device for measuring the contractile force of human-induced pluripotent stem cell (hIPSC)-derived cardiomyocytes. The device consists of two (1) 15 μm thick silicone cantilevers with (2) embedded gold-plated silver nanowire strain gauges.

hydrosilylation, and moisture curing.[9] Radical-mediated systems, including vinyl−vinyl[10] and thiol−ene reactions,[11−14] can be activated by UV exposure.[15] However, thin-film photopatterning studies of these materials typically require high exposure doses (3700−20,000 mJ cm^{-2}),[10,12] achieve minimum feature sizes on the order of ∼200 μm,[13] and report limited quantitative data on sidewall geometry or optical transmission. Oxygen inhibition and proprietary resin formulations further restrict practical implementation.

Two-part platinum-catalyzed hydrosilylation systems, in contrast, are mechanically tunable and widely available. These formulations consist of vinyl-functional PDMS, hydrosilane-functional PDMS, a platinum catalyst (often Karstedt's catalyst), a curing inhibitor, and reinforcing fillers such as fumed silica.[16] Mechanical properties can be adjusted via the base-to-cross-linker ratio without altering backbone chemistry. However, previous strategies to photopattern hydrosilylation silicones have generally relied on photodegradation of the platinum catalyst using shortwave UV (<365 nm).[17−19] Effective catalyst degradation typically requires exposure doses exceeding 7000 mJ cm^{-2} and produces features larger than 100 μm, with sidewall angles commonly in the range of 40°−60°.[10,20] These approaches therefore incur high dose requirements and limit achievable resolution while offering little control over final mechanical properties.

Extensive commercial and academic investigations of photoactivated platinum systems[21−27] have focused primarily on bulk curing kinetics, adhesion, or rheology rather than microstructure definition. As a result, systematic analyses of lithographic resolution, optical transmission, and sidewall fidelity remain sparse (Table S1).

Here, we introduce a distinct strategy: rather than photodegrading the catalyst or directly photoactivating cross-linking chemistry, we locally modulate curing kinetics by photodeactivating a cross-linking inhibitor. Building on our previous observation that UV exposure suppresses the reactivity of $FeCl_3$−polyether complexes during oxidative polymerization,[28] we hypothesized that an analogous approach could be applied to hydrosilylation-based silicones.

$FeCl_3$ inhibits platinum-catalyzed hydrosilylation, increasing the time required for curing. By combining $FeCl_3$ with a commercially available poly(ethylene oxide)−co−PDMS copolymer (PEO−PDMS), we create a photoresponsive inhibitor complex whose effectiveness decreases upon UV exposure. In this framework, UV light does not activate cross-linking directly; instead, it locally reduces inhibitor strength, generating spatial curing-rate contrast between exposed and unexposed regions.

Incorporating the $FeCl_3$−PEO−PDMS complex into commercially available two-part hydrosilylation silicones (e.g., Sylgard 184, Sylgard 527, Dragon Skin, and Ecoflex) enables reliable negative-tone photopatterning using low-dose 365 nm

https://doi.org/10.1021/acsapm.5c04718
ACS Appl. Polym. Mater. XXXX, XXX, XXX−XXX

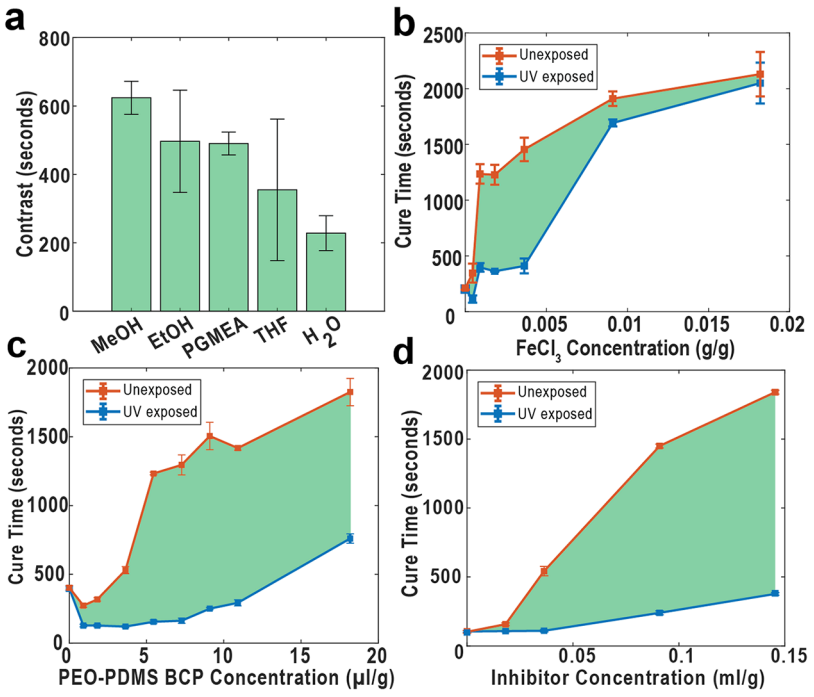

Figure 2. Photopatterning parameter space for Sylgard 184 formulations incorporating the photodeactivated inhibitor. All ratios are reported relative to the mass of silicone liquid used to prepare the elastomer. (a) Solidification times for UV-exposed and unexposed films prepared using different solvents in the photodeactivated inhibitor; the shaded region highlights the resulting solidification contrast, defined as the difference between unexposed and exposed solidification times. (b) Solidification times for UV-exposed and unexposed films as a function of $FeCl_3$ concentration at fixed (0.035 g/g) PEO−PDMS copolymer content and total inhibitor loading. (c) Solidification times for UV-exposed and unexposed films as a function of PEO−PDMS copolymer concentration at fixed $FeCl_3$ (0.035 g/g) content. (d) Solidification times for UV-exposed and unexposed films as a function of total photodeactivated inhibitor loading. At inhibitor loadings greater than 0.15 mL g^{-1}, formulation viscosity increased.

UV exposure. This approach preserves mechanical tunability via base-to-cross-linker ratio, maintains optical transparency in low-silica formulations, and retains the biocompatibility characteristic of commercial materials. Using this method, we demonstrate full-thickness patterning, microfluidic device fabrication, and cardiac microphysiological systems with integrated sensors.

2. RESULTS

A schematic summary of the photopatterning workflow is shown in Figure 1a. Liquid precursors of two-part, platinum-catalyzed hydrosilylation silicone elastomers were mixed according to manufacturer specifications and combined with a photodeactivated inhibitor consisting of $FeCl_3{\cdot}(H_2O)_6$ and a PEO−PDMS copolymer (Gelest DBE-712). Thin films were prepared by spin-coating to thicknesses of 2.5−15 μm and exposed to UV light through a photomask. Following exposure, samples were heated on a hot plate to induce selective solidification of exposed regions, and un-cross-linked material was removed by solvent washing.

This process produced patterned features in all platinum-catalyzed hydrosilylation-based silicone elastomers tested (Figure 1b−e) but was ineffective for nonhydrosilylation silicone formulations. Patterning was achieved using standard 365 nm illumination and exclusively commercially available components.

Because Sylgard 184 is the most widely used silicone elastomer in our laboratory and in the broader research community, initial optimization was performed using this formulation. The approach was then adapted, without full reoptimization, to additional silicone formulations including Sylgard 527, Dragon Skin, and Ecoflex. For Sylgard 184, optimal patterning was obtained using a photodeactivated inhibitor composed of 4 parts methanol, 0.5 parts $FeCl_3$, and 0.5 parts PEO−PDMS copolymer by mass. For most formulations, this solution was added at a ratio of 0.1 mL per gram of silicone liquid, while very soft formulations such as Sylgard 527 required reduced inhibitor loading (0.025 mL g^{-1}). In the following sections, we present the effects of formulation and processing parameters on patterning contrast, feature fidelity, and material compatibility.

2.1. Formulation and Processing Parameters Governing Patterning Contrast

Photopatterning performance was quantified using solidification contrast, defined as the difference in solidification time between UV-exposed and unexposed regions under identical thermal curing conditions. Using Sylgard 184 as a model system, formulation and processing parameters were systematically varied to identify conditions that maximized contrast while maintaining uniform film formation and reproducible pattern transfer.

2.1.1. Inhibitor Composition Effects on Solidification Contrast. The composition of the photodeactivated inhibitor strongly influenced solidification contrast (Figure 2a−d). When the solvent used to prepare the inhibitor was varied at fixed $FeCl_3$ and PEO−PDMS content, methanol produced the largest difference in solidification time between exposed and unexposed regions (Figure 2a). Other solvents resulted in reduced or inconsistent contrast.

At fixed PEO−PDMS content and total inhibitor loading, increasing the $FeCl_3$ concentration increased contrast up to an intermediate optimum (Figure 2b). At low $FeCl_3$ concen-

https://doi.org/10.1021/acsapm.5c04718
ACS Appl. Polym. Mater. XXXX, XXX, XXX−XXX

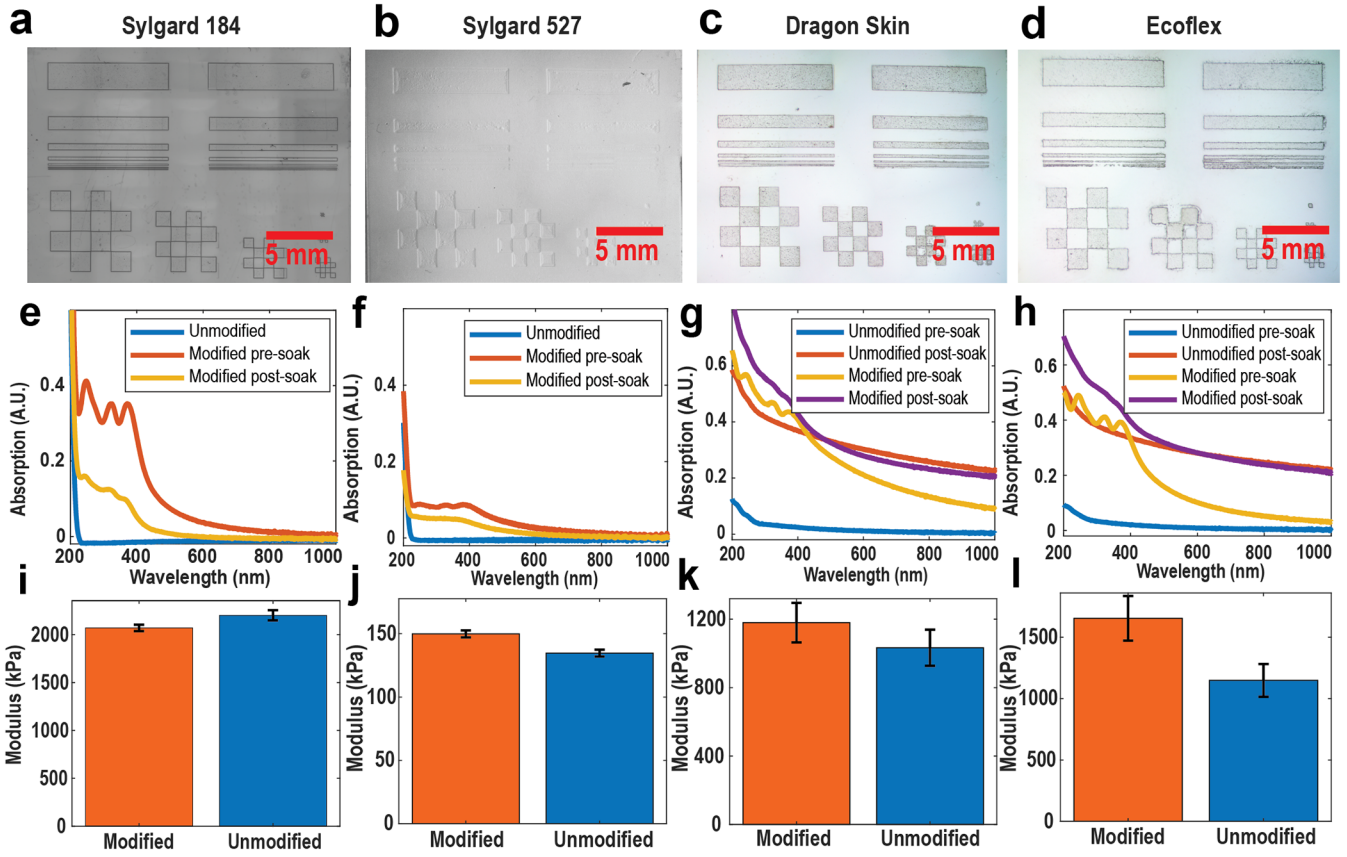

Figure 3. Optical and mechanical characterization of patterned silicone elastomers. (a–d) Stitched optical microscopy images of photopatterned films acquired under transmission illumination. (e–h) UV–vis transmittance spectra collected for unmodified and modified films before and after 2-propanol soaking. (i–l) Local elastic modulus measured by nanoindentation for unmodified and modified films. Unmodified samples correspond to silicone elastomers without added photodeactivated inhibitor; modified samples contain the photodeactivated inhibitor. (a) Sylgard 184. (b) Sylgard 527. (c) Dragon Skin 10 Medium. (d) Ecoflex 00–30. (e) Sylgard 184 UV–vis spectra. (f) Sylgard 527 UV–vis spectra. (g) Dragon Skin 10 Medium UV–vis spectra. (h) Ecoflex 00–30 UV–vis spectra. (i) Sylgard 184 nanoindentation modulus. (j) Sylgard 527 nanoindentation modulus. (k) Dragon Skin 10 Medium nanoindentation modulus. (l) Ecoflex 00–30 nanoindentation modulus.

trations, exposed and unexposed samples exhibited similar solidification times. At higher concentrations, solidification was delayed for both exposed and unexposed regions. A $FeCl_3$ concentration of 0.125 g g^{-1} relative to the PEO–PDMS content maximized contrast while maintaining reproducible curing behavior.

The presence of PEO–PDMS was required to produce a measurable contrast following UV exposure. At fixed $FeCl_3$ concentration, samples lacking PEO–PDMS showed no difference in solidification time between exposed and unexposed regions, whereas contrast increased with increasing PEO–PDMS concentration up to approximately 5 μL g^{-1} and then plateaued at higher loadings (Figure 2c).

Increasing the total inhibitor loading further increased contrast (Figure 2d). At loadings above 0.15 mL g^{-1}, the silicone liquid exhibited noticeable thickening, which limited uniform dispersion of additional inhibitor. Based on these trends, an inhibitor composition of 4 parts methanol, 0.5 parts $FeCl_3$, and 0.5 parts PEO–PDMS copolymer by mass was selected for subsequent experiments.

2.1.2. Mixing Conditions and Reproducibility of Patterning. Mixing conditions significantly affected patterning reproducibility. Short-duration, high-shear mixing produced visually uniform emulsions and consistent solidification contrast across repeated preparations. Using a custom overhead immersion mixer (Figure S1), mixing times below 30 s yielded reproducible curing behavior and reliable pattern transfer.

Lower-shear mixing methods, including magnetic stirring, required substantially longer mixing times (>10 min) and produced variable contrast and nonuniform patterning. All subsequent experiments therefore employed short-duration, high-shear mixing.

2.1.3. Exposure Geometry, UV Dose, and Film Thickness Dependence. Spatial resolution depended on UV exposure geometry, exposure dose, and film thickness. A fixed mask-to-substrate spacing was maintained using 3D-printed spacers (Figures S11–S12). As spacer height increased from 1.25 mm to 1.4 mm, measured sidewall angles decreased from approximately 59° to 35° (Figure S18).

Exposure doses required for full pattern transfer depended on silicone formulation and optical transparency. Using a 365 nm LED source (11.7 mW cm^{-2}), optimal doses ranged from 117–175 mJ cm^{-2} for transparent formulations (Sylgard 184 and Sylgard 527) and 351–468 mJ cm^{-2} for more optically opaque formulations (Ecoflex and Dragon Skin). After exposure, samples were thermally cured at 90 °C and developed using an ethyl acetate/IPA bath.

Decreasing film thickness consistently improved feature fidelity (Figure 1c,d). Across all tested formulations, films with thicknesses of approximately 2.5–15 μm could be patterned using the same exposure conditions.

https://doi.org/10.1021/acsapm.5c04718
ACS Appl. Polym. Mater. XXXX, XXX, XXX–XXX

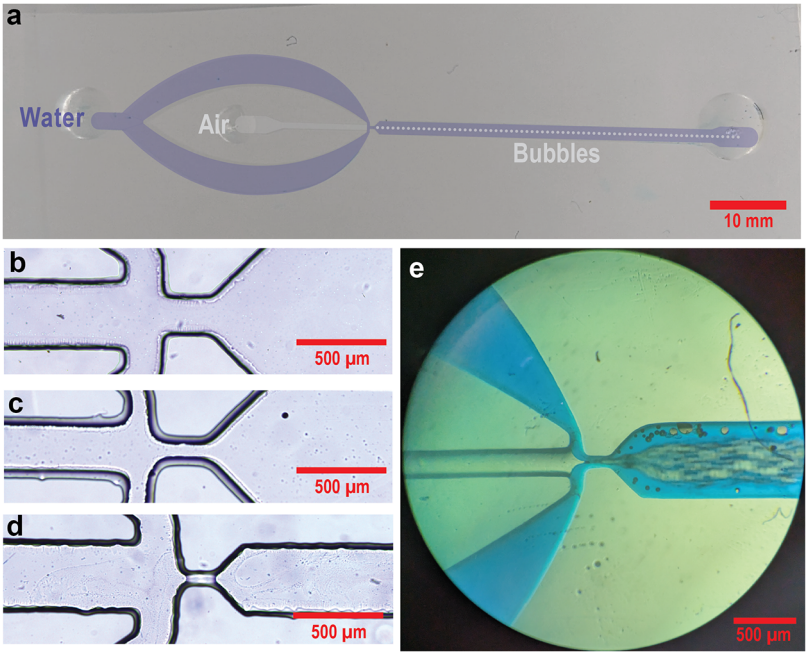

Figure 4. (a) Photograph of a microfluidic flow-focusing device fabricated using Sylgard 184 and our photodeactivated inhibitor. The liquid (blue) and gas (white) inlets, as well as the droplet formation region, are highlighted with a covered overlay. (b–d) Optical microscopy images of the flow-focusing junction with varying channel widths: (b) 200 μm, (c) 100 μm, and (d) 50 μm. (e) Optical microscopy image of the 100 μm channel generating a stream of bubbles.

2.1.4. Achievable Resolution and Sidewall Profiles. Using the optimized formulation and processing conditions, reproducible features with lateral dimensions down to 20 μm were obtained in Sylgard 184 films. Photomasks containing nominal 15 μm features were also evaluated; these features were typically not retained after development under otherwise identical conditions. Top-down optical microscopy confirmed that 20 μm line widths and a 30 μm pitch were reproduced within the resolution of the imaging method (Figure 1c,d), indicating minimal gross dimensional distortion under the reported processing conditions.

White-light interferometry measurements confirmed that patterned relief depths matched the initial film thickness across the tested range (Figures S4–S9). For films between approximately 2.5 and 15 μm thick, full-depth pattern transfer was achieved without increasing UV exposure dose, although thicker films required longer postexposure thermal curing.

2.2. Optical Properties of Patterned Silicone Films

2.2.1. UV–Vis Transmittance Before and After Patterning. Optical transparency of patterned silicone films was evaluated using UV–vis transmittance spectroscopy. Measurements were performed on both modified (with photodeactivated inhibitor) and unmodified films, before and after soaking in 2-propanol (Figure 3e–h).

For Sylgard 184 and Sylgard 527, the UV–vis spectra showed minimal change in transmittance after photopatterning and solvent treatment. In both formulations, transmittance remained high across the visible spectrum following the IPA soak. In contrast, Dragon Skin and Ecoflex films exhibited a substantial decrease in optical transmittance after solvent soaking, manifested as increased scattering and reduced visible-light transmission, independent of whether the photodeactivated inhibitor was present.

2.2.2. Formulation-Dependent Transparency Changes Following Development. Qualitative assessment of optical clarity and pattern fidelity was performed using stitched optical microscopy images acquired under transmission illumination (Figure 3a–d). Patterned Sylgard 184 and Sylgard 527 films appeared optically clear at the macroscale, with sharp feature contrast and uniform background transmission. In contrast, Dragon Skin and Ecoflex films displayed pronounced haze and reduced feature visibility following solvent development, consistent with the UV–vis transmittance measurements.

Together, these results demonstrate that optical transparency after photopatterning and development is strongly formulation-dependent. Transparent, dielectric silicones (Sylgard 184 and 527) retain high optical clarity under the reported processing conditions, while silica-filled elastomers (Dragon Skin and Ecoflex) undergo significant transparency loss following solvent exposure.

2.3. Mechanical Properties of Patterned Silicone Elastomers

2.3.1. Local Elastic Modulus by Nanoindentation. To assess whether photopatterning alters local mechanical response, the elastic modulus of patterned and unmodified silicone films was measured by nanoindentation under identical processing conditions (Figure 3i–l). For Sylgard 184 and Sylgard 527, the measured local elastic moduli of modified films closely matched those of the corresponding unmodified controls. Similar agreement was observed for Dragon Skin 10 Medium, while Ecoflex 00–30 exhibited a larger spread in measured values following photopatterning.

These measurements indicate that, at the length scale and deformation mode probed by nanoindentation, the local elastic response of the silicone network is largely preserved after incorporation of the photodeactivated inhibitor, particularly for lightly filled formulations.

2.3.2. Bulk Tensile Modulus of Modified and Unmodified Formulations. Bulk tensile properties were evaluated using water-supported tensile testing of thin films (Figure S13). This method enables mechanical characterization

https://doi.org/10.1021/acsapm.5c04718
ACS Appl. Polym. Mater. XXXX, XXX, XXX–XXX

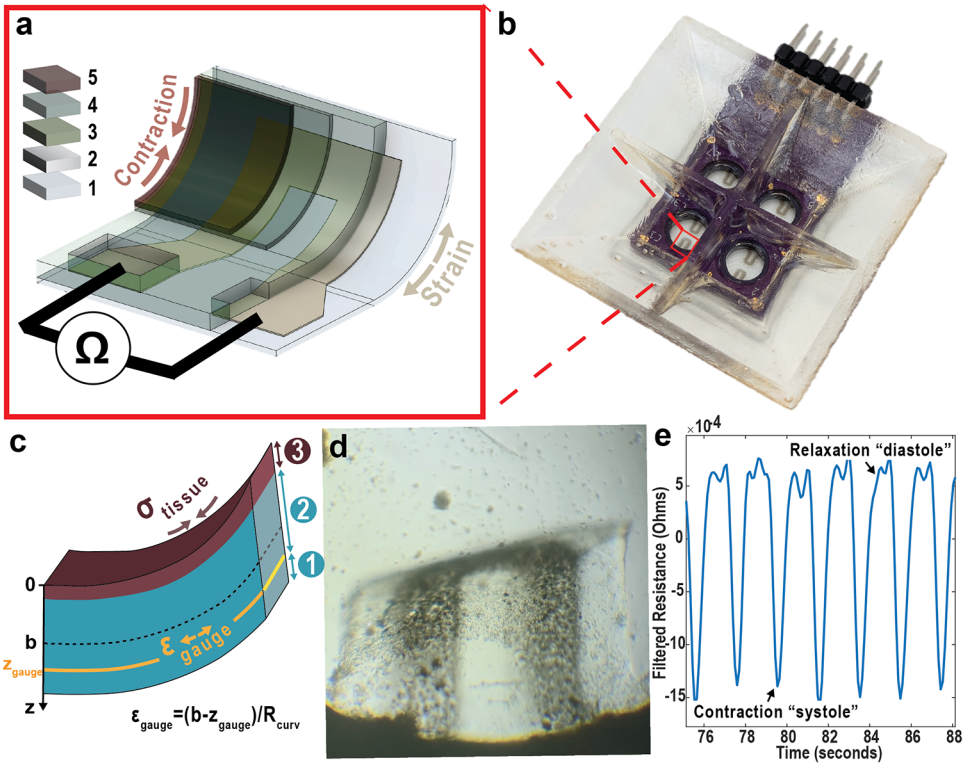

Figure 5. Device-level demonstration of a photopatterned PDMS cardiac microphysiological system. (a) Cross-sectional schematic of the photopatterned silicone cantilever device, consisting of: (1) an initial 2.5 μm thick layer of photopatterned silicone, (2) a strain gauge formed by spray-coated gold-plated silver nanowires, (3) a second 12.5 μm thick layer of photopatterned silicone, (4) a fibronectin coating to promote cell adhesion, and (5) a monolayer of hIPSC-derived cardiomyocytes. (b) Photograph of the assembled device. (c) Cross-sectional schematic of the cantilever structure used for mechanical analysis, showing the relative thicknesses of the two PDMS layers and the position of the hIPSC-derived cardiomyocyte microtissue. (d) Optical microscopy image of a cantilever supporting a contracting hIPSC-derived cardiomyocyte monolayer (see Video S1). (e) Processed resistance versus time signal acquired from the integrated gold-plated silver nanowire strain gauge during spontaneous cardiomyocyte contractions. Raw data and processing details are provided in the Supporting Information.

of soft, thin elastomeric films under conditions comparable to those used during photopatterning.

All formulations exhibited a reduction in tensile modulus following incorporation of the photodeactivated inhibitor. For Sylgard 184 (10:1), the tensile modulus decreased from 748 kPa (unmodified) to 205 kPa (modified). Dragon Skin 10 Medium decreased from 410 to 138 kPa, and Ecoflex 00−30 decreased from 117 to 70 kPa. Sylgard 527 and Sylgard 184 (30:1) were below the measurable range of the tensile testing setup.

These measurements demonstrate that incorporation of the photodeactivated inhibitor affects bulk mechanical behavior across all formulations tested, with the magnitude of softening dependent on the base elastomer.

2.4. Biocompatibility Assessment

Biocompatibility of Sylgard 184 modified with the $FeCl_3$−PEO photodeactivated inhibitor was evaluated using U2OS cells cultured on modified and unmodified substrates.[29] Prior to cell culture, all substrates were soaked in 2-propanol for ∼72 h to remove un-cross-linked silicone components and residual photodeactivated inhibitor.

Cell morphology, adhesion, and proliferation were assessed by fluorescence microscopy following staining with DAPI (nuclei) and phalloidin (F-actin) (Figure S14). Quantitative image analysis was performed using ImageJ (NIH). Nuclei were counted from DAPI-stained images to determine areal nuclear density, and surface confluence was calculated as the thresholded area fraction. Cells cultured on modified and unmodified substrates exhibited comparable morphologies, characterized by flattened, spread cell bodies with well-defined actin cytoskeletons and intact nuclei.

Nuclear density on unmodified substrates was 3.4×10^4 nuclei cm^{-2}, while modified substrates exhibited 4.6×10^4 nuclei cm^{-2}. Corresponding surface confluence values were 64% on unmodified substrates and 84% on modified substrates. No evidence of widespread cell detachment, rounding, or loss of adhesion was observed on either substrate type, indicating that modified Sylgard 184 supports cell attachment and proliferation under the conditions tested.

2.5. Device-Level Demonstrations

2.5.1. Microfluidic Device Fabrication and Operation.

To evaluate the ability of the photopatterning process to produce functional microscale fluidic structures, a single-layer flow-focusing microfluidic device was fabricated using photopatterned Sylgard 184. The device incorporated lateral channel dimensions down to 50 μm (Figure 4d).

Upon operation, the device generated a continuous stream of bubbles using converging air and water inlets (Figure 4a). Stable flow-focusing behavior was observed across multiple devices, indicating that the patterned channels were mechanically robust and fluidically continuous under the applied flow conditions. These results demonstrate that photopatterned PDMS can support common microfluidic architectures with sub-100 μm critical dimensions.

https://doi.org/10.1021/acsapm.5c04718
ACS Appl. Polym. Mater. XXXX, XXX, XXX−XXX

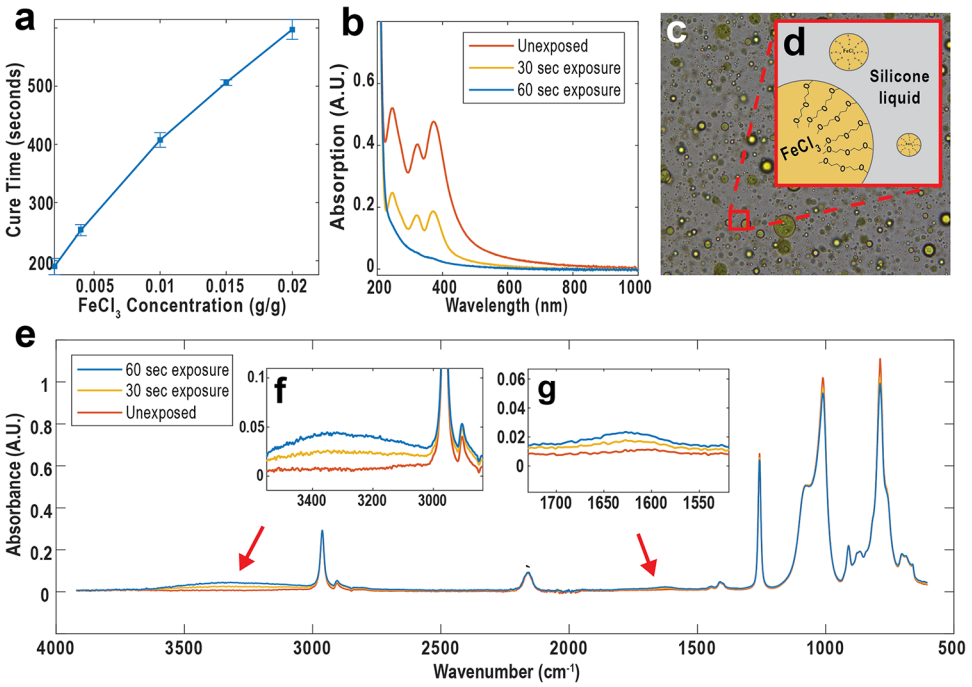

Figure 6. (a) The cure time of the silicone elastomers increases with the addition of $FeCl_3$ to the formulation. (b) UV−vis spectroscopy data showing the photochromic properties of the film. The disappearance of absorption peaks at 245, 325, and 374 nm suggests a reduction in higher-order $FeCl_4^-$ complexes in the film. (c) A photograph of the $FeCl_3$ and PEO−PDMS emulsion present in the film. The image was taken from a sample with large droplet sizes due to microscope resolution limitations. See SI for images of properly mixed emulsions. (d) An illustration depicting the $FeCl_3$ and PEO−PDMS emulsion, with PEO chains interacting with the emulsion interior. (e) Fourier transform infrared spectroscopy (FTIR) data of the custom silicone formulation with the photodeactivated inhibitor. The appearance of new peaks at 3400 cm^{-1} and 1630 cm^{-1} indicates the formation of PEO oxidation products. (f) The peak at 3400 cm^{-1} is associated with the formation of OOH/OH groups. (g) The peak at 1630 cm^{-1} corresponds to the formation of additional C−O bonds.

2.5.2. Cardiac Microphysiological System Fabrication and Function. To assess performance under biologically demanding conditions, the photopatterning process was applied to the fabrication of a cardiac microphysiological system based on muscular thin films integrated with strain sensors. The device architecture consisted of photopatterned PDMS cantilevers with integrated gold-plated silver nanowire strain gauges and supported monolayers of human induced pluripotent stem cell-derived cardiomyocytes (hIPSC-CMs) (Figure 5a−c).

Following fabrication and postpatterning extraction, cardiomyocytes were successfully seeded and maintained on the devices. Beating activity was observed in multiple wells within 2 days of seeding, and robust cantilever motion was detected by day three (Video 1). Electrical resistance measurements from the integrated strain gauges captured time-resolved contractile activity during beating (Figure 5e).

By day five postseeding, all 22 wells exhibited beating cardiomyocyte monolayers. By day nine, the fraction of beating wells decreased to 36%, accompanied by reduced contractile amplitude. These observations establish that photopatterned PDMS structures can support functional cardiac microtissues and integrated sensing under the conditions tested.

2.5.3. Fabrication Workflow and Integration. The cardiac microphysiological devices were fabricated using a multilayer photopatterned PDMS process. A 2.5 μm thick base layer formed the cantilever substrate and supported spray-coated gold-plated silver nanowire strain gauges. A second 12.5 μm thick photopatterned PDMS layer encapsulated the sensors and completed the mechanical structure. Devices were mounted on a printed circuit board (PCB) using silver epoxy and NOA 81 to establish electrical and fluidic interfaces.

Prior to cell seeding, devices were soaked in 2-propanol for 1−3 weeks (set by fabrication and assembly cadence) to remove residual inhibitor and un-cross-linked PDMS, followed by air plasma treatment and fibronectin coating to promote cell adhesion. Human iPSC-derived cardiomyocytes were seeded at a density of 468,750 cells cm^{-2} and cultured directly on the photopatterned cantilevers.

2.6. Exploration of the Photodeactivated Inhibition Mechanism

2.7. Cure-Time Modulation by $FeCl_3$ and UV Exposure

The addition of $FeCl_3$ to platinum-catalyzed hydrosilylation-based silicone formulations resulted in a pronounced increase in solidification time across all systems examined (Figure 6a). This behavior was observed for both commercial and custom-formulated silicones, indicating that $FeCl_3$ functions as an effective inhibitor of hydrosilylation under the processing conditions used.

When films containing both $FeCl_3$ and PEO−PDMS were exposed to 365 nm UV illumination prior to thermal curing, solidification times were significantly reduced relative to unexposed controls. This reduction in cure time was not observed in formulations lacking PEO, demonstrating that the presence of the polyether component is required to enable UV-induced deinhibition.

In a simplified custom silicone formulation comprising vinyl-terminated PDMS, a hydride-functional PDMS cross-linker, and a platinum catalyst, curing occurred within 105 s in the absence of inhibitor. Addition of the $FeCl_3$−PEO−PDMS inhibitor increased the cure time to approximately 88 min. Upon UV exposure, films containing both inhibitor and platinum catalyst

https://doi.org/10.1021/acsapm.5c04718
ACS Appl. Polym. Mater. XXXX, XXX, XXX−XXX

solidified in 40 ± 11.5 s, while unexposed films solidified in 112.5 ± 26.3 s under identical thermal conditions. These results establish that UV exposure reproducibly reduces the inhibitory effect of $FeCl_3$ in the presence of PEO−PDMS, leading to accelerated hydrosilylation relative to unexposed controls.

2.8. Spectroscopic Changes Following UV Irradiation

UV−vis spectroscopy was used to characterize optical changes in films containing $FeCl_3$ and PEO−PDMS before and after UV exposure (Figure 6b). Prior to illumination, films exhibited absorption features characteristic of Fe(III)−chloride complexes in the 300−400 nm range. Following UV irradiation, these absorption bands diminished substantially, indicating a significant change in the electronic state or coordination environment of the iron species present in the film.

Fourier transform infrared (FTIR) spectroscopy was employed to probe chemical changes within the silicone matrix following UV exposure (Figure 6e−g). After irradiation, new spectral features emerged at approximately 3400 cm^{-1} and 1630 cm^{-1}. These features were not present in unexposed films and were consistently observed in formulations containing both $FeCl_3$ and PEO−PDMS.

No resolvable changes in Si−H or vinyl group absorption were detected under the experimental conditions accessible in this work. The weak absorbance of these functional groups in thin silicone films, combined with the presence of overlapping polyether and PDMS vibrational modes, limited the sensitivity of FTIR measurements for direct kinetic tracking of hydrosilylation conversion.

3. DISCUSSION

Poly(dimethylsiloxane) (PDMS) can be patterned using a variety of subtractive and additive techniques. However, patterning thin, freestanding films imposes constraints that are not encountered in bulk molding or embossing. At film thicknesses relevant to microfluidic and bioMEMS devices, patterning processes must provide full-thickness feature definition, while maintaining film uniformity, dimensional accuracy, and predictable mechanical properties after curing. Approaches that substantially alter the curing chemistry or introduce additional cross-linking pathways can compromise these requirements by changing optical transmission, mechanical response, or process robustness across the film.

The problem addressed here is not how to replace platinum-catalyzed hydrosilylation with a light-initiated cross-linking chemistry, but how to introduce light-responsive control over cure kinetics in thin films of a liquid precursor while retaining the accessibility and tunability of established hydrosilylation-based elastomers. Spatial definition is achieved by introducing a photomodulated kinetic asymmetry into an otherwise conventional curing system. Incorporation of a photodeactivated $FeCl_3$−PEO−PDMS inhibitor complex produces formulations in which UV exposure locally reduces inhibition, allowing exposed regions to advance toward mechanical stability while unexposed regions remain fluid and removable. UV exposure does not initiate cross-linking or generate a secondary polymer network; instead, it shifts the local balance between inhibition and thermally driven hydrosilylation.

Under this framework, pattern fidelity in thin PDMS films is determined by the competition between formulation-dependent cure kinetics and spatially nonuniform optical dose. Inhibition strength and photodeinhibition efficiency set the achievable separation in solidification times (Figure 6), while exposure geometry, mask-to-film spacing, and optical transport in a multiphase, scattering medium define the dose gradients that control sidewall angle and resolution. These coupled effects account for the observed dependence of sidewall inclination on exposure conditions, the reproducible ∼15−20 μm resolution limit under the conditions reported here (Figure 1c,d), and the formulation-dependent trade-offs between optical transparency, mechanical robustness, and pattern fidelity (Figure 2).

3.1. Design and Physical Constraints Governing Photodeactivated PDMS Patterning

Among reported approaches for directly photopatterning silicone elastomers, exposure dose, achievable resolution, and materials generality vary widely depending on the underlying chemistry (Table S1). Systems based on photo-cross-linking mechanisms such as thiol−ene or epoxy chemistry can achieve rapid curing, but often require substantial reformulation of the base elastomer and exposure doses in the multijoule-per-square-centimeter range, with feature sizes typically 100 μm. Prior demonstrations specifically relying on catalyst photodeactivation to pattern hydrosilylation-based silicones have likewise required high UV doses and have been limited in resolution or formulation flexibility.

In contrast, the approach presented here enables reproducible patterning of commercially available platinum-cured PDMS formulations using standard 365 nm illumination at exposure doses below 200 mJ cm^{-2} for transparent systems, while achieving feature sizes down to ∼20 μm and sidewall angles approaching 60° (Table S1). This represents an order-of-magnitude reduction in exposure dose relative to prior catalyst-deactivation approaches, without the need for custom catalysts, oxygen exclusion, or proprietary resin systems.

Rather than introducing new cross-linking chemistries, spatial selectivity is achieved by locally modulating the cure kinetics of an otherwise conventional hydrosilylation reaction. As discussed below, this kinetic mode of patterning enables broad compatibility with widely used silicone elastomers while also introducing practical constraints associated with multiphase formulations, liquid precursors, and noncontact exposure geometries.

3.1.1. Kinetic Selectivity via Photodeactivated Inhibition of Hydrosilylation. Unlike conventional photoresist or photo-cross-linking systems, the photopatterning approach used here does not rely on irreversible bond formation or cleavage to define patterned regions. Instead, spatial selectivity is achieved by locally modulating the cure rate of a standard platinum-catalyzed hydrosilylation reaction through reversible catalyst inhibition. This distinction is critical for maintaining compatibility with commercially available platinum-cured silicone elastomers, which are formulated to cure thermally rather than photochemically.

Pattern fidelity in this system is therefore governed by the difference in curing behavior between exposed and unexposed regions. UV exposure does not directly initiate cross-linking; rather, it accelerates curing by reducing the inhibitory effect of the $FeCl_3$−PEO complex. As a result, exposed regions advance toward mechanical stability while unexposed regions remain fluid for a longer period and can be selectively removed during development. In practical terms, successful patterning requires a sufficiently large separation in solidification time between these two regions. This solidification-time contrast defines the usable processing window and directly determines whether patterned features can be retained without distortion or collapse.

https://doi.org/10.1021/acsapm.5c04718
ACS Appl. Polym. Mater. XXXX, XXX, XXX−XXX

Importantly, curing in the exposed regions proceeds through the same hydrosilylation chemistry used in conventional thermal processing. Because no secondary polymer network is introduced and no permanent photoreactive groups are incorporated, the intrinsic mechanical, optical, and biological properties of the base silicone elastomer are largely preserved after patterning.

Reversible catalyst inhibition is thus the primary mechanism enabling pattern formation. By separating photoresponse from network formation, the method avoids oxygen-sensitive radical chemistry, custom catalyst synthesis, or extensive reformulation of the base resin. All reactive components are commercially available and commonly used in silicone processing, allowing photopatternability to be introduced without fundamentally changing the underlying material system.

To maximize solidification-time contrast, we optimized formulation and processing parameters empirically using a one-variable-at-a-time (OVAT) approach. While this strategy does not capture coupled or nonlinear interactions between parameters, it provided clear physical intuition and robust operating conditions across multiple commercial silicone formulations. More comprehensive multivariate optimization (e.g., factorial design-of-experiments) could further refine the parameter space, but such an effort was beyond the scope of this application-driven study.

3.1.2. Multiphase Inhibitor as an Enabler and Limiting Factor. A key aspect of this photopatterning method is the use of a multiphase formulation, in which polar $FeCl_3$−PEO inhibitor domains are dispersed within a nonpolar silicone matrix (Figure 5c,d). This emulsion-based approach allows inorganic salts and polyether components to be incorporated into commercial silicone formulations that would otherwise be incompatible with homogeneous mixing. In practice, this enables photopatterning across a range of platinum-cured elastomers without reformulating the base resin or altering the underlying curing chemistry.

The PEO−PDMS block copolymer plays a dual role in this process. It stabilizes the polar, inhibitor-containing domains while remaining compatible with the silicone precursor, allowing the inhibitor to be dispersed uniformly without visible phase separation. This amphiphilic structure is essential for maintaining reproducibility across batches and for extending the method to different commercial silicone kits.

We found that the size and quality of the emulsion had a strong impact on patterning performance. Because both inhibition and UV-induced deinhibition are expected to occur primarily at the interfaces between the inhibitor droplets and the surrounding silicone, finer emulsions consistently produced higher solidification-time contrast and more reliable pattern transfer. In contrast, poorly dispersed formulations showed greater variability in curing behavior and reduced reproducibility, even when nominal compositions were identical. Achieving a sufficiently fine emulsion therefore required short, high-shear mixing, consistent with a surface-mediated reaction pathway.

At the same time, the presence of dispersed inhibitor domains introduces inherent optical trade-offs. The internal phase boundaries act as scattering centers under UV illumination, broadening the effective exposure profile and contributing to the rounded edges and sloped sidewalls observed at small feature sizes. These effects are not primarily due to process instability but are intrinsic to embedding photoreactive domains within an otherwise optically transparent elastomer.

As a result, patterning performance in this system reflects a balance between chemical accessibility and optical precision. The multiphase formulation enables broad compatibility with widely used silicone elastomers but imposes predictable limits on resolution and sidewall sharpness. Within these constraints, control over droplet size and dispersion uniformity—through formulation and mixing—emerges as a practical lever for optimizing contrast and pattern fidelity.

3.1.3. Exposure-Tool Compatibility with Liquid and Soft Polymer Precursors. Photopatterning PDMS and related soft-polymer systems imposes constraints that differ fundamentally from those encountered in conventional photoresist processing. Before curing, PDMS precursors are low-viscosity liquids, and even after partial curing or at very low moduli, the material remains highly compliant and tacky. This physical state is incompatible with contact or near-contact exposure workflows designed for solvent-depleted, mechanically stable photoresist films. Direct contact between the photomask and the uncured film can readily distort the coating, contaminate the mask, or introduce uncontrolled and spatially varying gaps that degrade pattern fidelity. In extreme cases, the photomask can adhere to the uncured or partially cured film, leading to sticking/tearing on separation and lateral squeeze-out of the liquid precursor, which both destroys pattern fidelity and risks contaminating or damaging the mask.

For this reason, maintaining a finite and well-defined mask-to-film separation is not a unique requirement of the photodeactivated hydrosilylation chemistry introduced here, but rather a general constraint when patterning liquid or ultrasoft polymer precursors using mask-based illumination. In practice, this separation was enforced using a simple spacer-based air-gap fixture fabricated by 3D printing (Figure S11), which allows the standoff distance between the photomask and the film surface to be set reproducibly. Spacer heights ranging from 1.1 to 1.4 mm were used in this work, providing controlled variation in exposure geometry while avoiding mechanical contact with the uncured silicone film.

The spacer fixture should therefore be viewed as an interface solution that enables compatibility between soft-matter precursors and standard photomask exposure tools, rather than as a process-specific limitation. As discussed in the following section, the imposed air gap directly influences sidewall geometry and resolution through geometric beam spreading and diffraction; however, it also enables reliable exposure of liquid films that would otherwise be difficult or impossible to pattern using conventional contact lithography. Fully noncontact exposure approaches (e.g., projection lithography or digital micromirror-based systems) would remove this constraint entirely, while remaining fully compatible with the underlying photodeactivated inhibition mechanism.

3.1.4. Resolution Limits and Sidewall Geometry. Once a finite mask-to-film separation is imposed, feature fidelity is primarily determined by the exposure geometry. In practice, the final pattern shape reflects the combined effects of geometric beam spreading, diffraction across the air gap, light scattering within the multiphase film, and the time required for exposed regions to reach mechanical stability before development. Under these conditions, the distance between the photomask and the film surface becomes the dominant parameter controlling sidewall angle and the achievable lateral resolution.

As observed experimentally, increasing the mask-to-film separation systematically reduced sidewall angles (Figure S18). This trend is consistent with simple geometric divergence

https://doi.org/10.1021/acsapm.5c04718
ACS Appl. Polym. Mater. XXXX, XXX, XXX−XXX

and diffraction of the incident UV light across the air gap. In the present multiphase formulations, these effects are further amplified by scattering from the dispersed inhibitor domains, which broadens the effective exposure profile near feature edges. The resulting dose gradients are therefore softer than those obtained in single-phase photoresist systems, leading to rounded edges and sloped sidewalls at small feature sizes. As discussed above, the need for a controlled air gap arises from the physical state of the uncured silicone and should be viewed as a general consequence of patterning liquid or ultrasoft polymer films using mask-based illumination.

Under the exposure conditions reported here, the practical lateral resolution limit was approximately 15−20 μm. Features designed below this scale were typically not retained after development, not because of edge distortion, but because partially illuminated regions did not cure rapidly enough to become mechanically stable. This behavior defines a clear and reproducible cutoff governed by solidification-time contrast, rather than a gradual loss of dimensional accuracy with decreasing feature size.

In the present multiphase formulations, solvent redistribution and evaporation likely occur during casting, exposure, and the earlier stages of cross-linking; however, we did not directly measure solvent retention or the time course of solvent removal during cure. As a result, we cannot rule out a contribution of late-stage solvent loss to the final feature profile. Because solvent removal, curing kinetics, and mechanical stabilization occur on overlapping time scales, any solvent-related deformation would be difficult to decouple from other factors that influence sidewall slope and edge rounding, including exposure dose gradients, light scattering, and delayed solidification near feature boundaries. We therefore treat solvent-related effects as a secondary, coupled contribution to feature evolution, rather than as an independently resolved or dominant limit on achievable resolution under the conditions studied.

Dimensional fidelity was evaluated by comparing patterned structures to the corresponding photomask designs using top-down optical microscopy. Masks containing 20 μm lines with a 30 μm pitch consistently produced patterned features with comparable line widths and spacing within the resolution limits of optical microscopy (Figure 1c,d). In contrast, features designed at 15 μm were generally removed during development, consistent with the resolution limit described above. Quantitative measurement of line-edge roughness or sidewall roughness was not pursued because the cured PDMS features are optically transparent and provide limited intrinsic contrast after development, making robust edge detection by optical microscopy unreliable. SEM-based metrology was also found to be impractical for these thin, compliant microfeatures, as conductive coating and vacuum exposure introduced visible deformation.

Compared to single-phase photopatternable systems—such as homogeneous photo-cross-linkable networks or polymer-bound photoacid generators—the present approach trades ultimate resolution for formulation flexibility and process simplicity. Single-phase systems can sustain sharper dose gradients and steeper sidewalls, but typically require custom polymer synthesis, restricted material choices, or aggressive exposure conditions that are incompatible with many commercial silicone elastomers. In contrast, the multiphase photodeactivated hydrosilylation strategy enables low-dose patterning of widely used platinum-cured silicones, accepting moderate resolution limits as a practical trade-off.

These considerations also motivate the focus on thin silicone films (2.5−15 μm) in this work. Within this thickness range, optical attenuation, scattering, and diffusion-related broadening are minimized while remaining well matched to the intended applications, such as compliant microphysiological cantilevers, thin membranes, and patterned structuring layers. In preliminary experiments with thicker films (15 μm), coating nonuniformity and edge-bead formation increased the required mask-to-film separation and led to degraded resolution and sidewall fidelity. While extension of this approach to substantially thicker films (e.g., 100−500 μm) is feasible in principle, it would require dedicated optimization of thick-film processing and noncontact exposure strategies and is therefore beyond the scope of the present study.

3.2. Optical Transparency and Solvent−Filler Interactions

The observed differences in optical behavior between silicone formulations arise primarily from formulation chemistry rather than from the photopatterning process itself (Figure 3a−h). Sylgard 184 and Sylgard 527 are lightly filled or unfilled dielectric elastomers, and their optical clarity is therefore largely preserved following incorporation and removal of the photodeactivated inhibitor. In these systems, IPA soaking effectively removes residual $FeCl_3$ and PEO−PDMS without introducing persistent scattering centers, enabling recovery of high transparency.

By contrast, Dragon Skin and Ecoflex contain high loadings of fumed silica fillers that are integral to their mechanical performance. Exposure to organic solvents disrupts the filler−polymer network, leading to irreversible microstructural rearrangements that increase light scattering. The fact that similar transparency loss is observed in unmodified samples subjected to identical solvent treatment indicates that this effect is intrinsic to the base formulation rather than a consequence of inhibitor chemistry.

These results highlight an important constraint imposed by commercial filler loading: while silica-filled elastomers are mechanically robust and widely used, their resistance to solvent-based development processes is limited. As a consequence, optical transparency and high-resolution feature fidelity are more readily preserved in lightly filled or unfilled silicone formulations under the present processing conditions.

From an application perspective, these distinctions inform selection of target use cases. Transparent formulations such as Sylgard 184 and 527 are well suited for optically interrogated microfluidic devices, thin-film MEMS structures, and bio-interfaces requiring visual access. In contrast, silica-filled elastomers may remain appropriate for applications where optical clarity is noncritical, but alternative development strategies or solvent systems would be required to mitigate transparency loss.

3.3. Mechanical Property Preservation across Length Scales

A central motivation for patterning commercial platinum-cured silicones is that these materials are selected not only for process familiarity, but for their uniquely tunable compliance and well-established performance in optical and biological interfaces. Introducing photopatternability is therefore only useful if it does not catastrophically alter the mechanical response that makes these elastomers attractive in the first place. Our mechanical measurements were chosen to probe this question across relevant length scales: local response within thin patterned films and microfeatures, and film-scale tensile response in mechanically relevant thin specimens.

https://doi.org/10.1021/acsapm.5c04718
ACS Appl. Polym. Mater. XXXX, XXX, XXX−XXX

3.3.1. Elastic Response across Length Scales. The combined nanoindentation and tensile data reveal a length-scale-dependent elastic response upon incorporation of the photodeactivated inhibitor emulsion. Nanoindentation probes small volumes at short time scales and is therefore sensitive to local network integrity within cured regions. For transparent, lightly filled formulations (e.g., Sylgard 184 and Sylgard 527), the effective elastic modulus measured by nanoindentation remains close to that of unmodified controls, indicating that local hydrosilylation curing and stiffness at the feature scale are largely preserved following photopatterning (Figure 2i–l).

In contrast, silica-filled elastomers (e.g., Dragon Skin and Ecoflex) exhibit substantially higher point-to-point variability in nanoindentation measurements. We attribute this dispersion to development-induced microstructural heterogeneity: exposure to solvent during development perturbs the filler–polymer network and can locally redistribute or partially extract filler-rich domains, producing spatially heterogeneous stiffness on the indentation length scale. In this regime, nanoindentation captures real local variations in composite microstructure rather than measurement noise, consistent with the formulation-dependent optical scattering changes observed after solvent processing.

To probe mechanical response at a larger (film) length scale, we performed tensile testing on thin-film specimens using a water-assisted tensile method. While these measurements still reflect the mechanics of thin films rather than bulk cast elastomers, they integrate deformation over millimeter-scale gauge lengths and are sensitive to film-scale network connectivity and heterogeneity that are not captured by localized indentation. Across all formulations, these tensile measurements show a reduction in tensile modulus upon inhibitor addition, consistent with a decrease in effective cross-link density and/or increased network heterogeneity introduced by the dispersed inhibitor phase. Importantly, this softening does not preclude fabrication of mechanically robust microstructures; rather, it primarily shifts the overall compliance of thin-film elements. From a device-design perspective, this distinction is consequential: local stiffness governs feature integrity, dimensional stability, and resistance to collapse during development, whereas the film-scale tensile modulus more directly sets the compliance of cantilevers, membranes, and other mechanically active elements fabricated in this thickness regime. Consistent with this interpretation, the measured variability in tensile modulus remains small relative to the absolute change in stiffness (Figure S13), supporting reproducible device fabrication even as global (film-scale) compliance is altered.

3.3.2. Time-Dependent Mechanics and Cyclic Loading. For applications involving cyclic actuation, damping, or long-term dimensional stability, frequency-dependent viscoelastic properties—including the storage modulus (E'), loss modulus (E''), and loss tangent ($\tan\delta$)—can become important alongside quasi-static elastic metrics. In many PDMS formulations at standard mixing ratios, the response is often reported to be predominantly elastic over practical measurement conditions, although measurable rate- and frequency-dependent behavior can still arise depending on formulation, cross-linking, and test conditions.[30] In hydrosilylation-cured silicones more broadly, dynamic response is expected to depend on cross-link density and network structure, and thus could plausibly be perturbed by multiphase inhibitor emulsions that also measurably reduce thin-film tensile modulus in our experiments.

At the device level, the extent to which full viscoelastic modeling is required depends on the intended operating regime and the magnitude of deformation. Lin et al. developed a viscoelastic force-conversion framework for PDMS microcantilevers and showed that, for representative small deformations, elastic and viscoelastic finite-element force conversions differed by only ∼0–11% depending on strain rate, with larger discrepancies at larger deformations.[31] This result suggests that, for many microphysiological cantilever use cases where biological and material variability dominates the error budget, an elastic approximation may be sufficient for force conversion over typical operating conditions, while viscoelastic characterization becomes more critical when pushing to higher frequencies, larger deformations, or when quantitative damping/creep limits are required.

In the present manuscript, the cardiac microphysiological cantilever platform serves as a device-level demonstration that photopatterned commercial silicone can support demanding biological operation while enabling functional readout of contractility over the experimental time window studied. With respect to lifetime under cyclic loading, Kim et al. reported stable operation of a PDMS-encapsulated crack-sensor integrated silicone-rubber cantilever for up to 26 days (>5 × 10^6 heartbeats) and observed no change in gauge factor attributable to fatigue fracture even after five million repeated cycles.[32] While such results support the feasibility of robust long-duration cyclic operation in silicone cantilever systems, systematic lifetime characterization specific to inhibitor-modified thin films (e.g., DMA-derived E', E'', and $\tan\delta$ across formulations/loadings, creep under sustained stress, and fatigue under controlled cyclic loading in physiologically relevant environments) constitutes a distinct study and was therefore not undertaken here. Extending mechanical characterization to these protocols represents a natural direction for future work, particularly for applications requiring long-duration cyclic actuation and quantitative stability limits.

In addition to purely viscoelastic considerations arising from network structure and cross-link density, long-term mechanical stability of silicone elastomers may also be influenced by slow chemical processes that modify the siloxane backbone over extended time scales. $FeCl_3$ is a Lewis-acidic salt, and iron(III) halides have been reported to catalyze siloxane bond cleavage, redistribution, or depolymerization under sufficiently forcing conditions. In particular, iron-catalyzed depolymerization of poly(dimethylsiloxane) has been demonstrated in chemical-recycling contexts employing high catalyst loadings (often 5 mol %), elevated temperatures (typically ∼180–200 °C), and excess reagents such as alcohols (e.g., methanol or long-chain fatty alcohols) to drive siloxane scission and equilibrium redistribution.[33−35] Related studies on silicone degradation more broadly have likewise emphasized the strong dependence of siloxane bond cleavage on temperature, chemical environment, and catalyst accessibility.[36]

While these literature precedents establish a plausible chemical pathway for Si–O bond scission in the presence of iron salts, the relevant regimes differ substantially from those explored in the present work. In inhibitor-modified PDMS films processed and evaluated near ambient conditions, any residual Fe/Cl species remaining after solvent extraction are expected to be present at low concentration and largely immobilized within a cross-linked network, limiting catalytic accessibility and reaction

https://doi.org/10.1021/acsapm.5c04718
ACS Appl. Polym. Mater. XXXX, XXX, XXX−XXX

kinetics on experimental time scales. Nevertheless, prolonged exposure to elevated temperature, humidity, or solvent-rich environments could, in principle, accelerate slow siloxane scission or network rearrangement, potentially manifesting as gradual changes in viscoelastic response (e.g., increased creep, dissipation, or drift in effective modulus). Systematic evaluation of such long-time scale chemical and mechanical aging effects—via accelerated aging and dynamic mechanical analysis—constitutes a distinct study and was therefore not undertaken here.

3.4. Biocompatibility in Structurally and Biologically Demanding Interfaces

A key outcome of this work is that photopatterned commercial silicone produced by our method can support biologically demanding device operation. In particular, we successfully integrated photopatterned Sylgard 184 into cardiac microphysiological cantilever devices supporting human induced pluripotent stem cell-derived cardiomyocytes (hIPSC-CMs) (Figure 4), enabling robust early beating and functional contractility readout over the primary experimental window studied here.

Consistent with this device-level demonstration, we also observed no detectable differences in cell morphology, adhesion, or proliferation between modified and unmodified Sylgard 184 substrates using U2OS cells as a robust screen for gross cytocompatibility. These results are notable given the incorporation of redox-active species during photopatterning: $FeCl_3$ and polyether components are known to participate in oxidative and radical-driven processes during UV exposure, yet they do not appear to persist at levels that elicit a detectable cytotoxic response after postpatterning treatment under the conditions studied here.

The effectiveness of the solvent extraction step is therefore critical. Such solvent extraction or leaching steps are standard practice for PDMS substrates intended for cell culture, where removal of un-cross-linked oligomers and low−molecular-weight species is known to improve cytocompatibility.[37,38] In the present work, soaking in 2-propanol removes residual inhibitor components and un-cross-linked silicone oligomers, yielding surfaces that are comparable to unmodified controls from a cellular response perspective. This outcome is consistent with the optical and mechanical data, which indicate that postprocessing restores key material properties in lightly filled formulations. Nonetheless, high-sensitivity surface and near-surface compositional analysis (e.g., XPS and/or ToF-SIMS targeting Fe and Cl) would be valuable in future work to directly quantify any residual inhibitor-derived species after extraction and to establish quantitative cleanliness limits across formulations and inhibitor loadings.

We note that the reduced prevalence of beating observed after day 9 should not be interpreted as evidence of material toxicity without controlled longitudinal isolation of confounding variables. Long-duration hiPSC-CM function in vitro is widely reported to be highly sensitive to culture conditions and to evolve over time in a multifactorial manner, including culture-duration−dependent maturation and ensemble dynamics (e.g., shifts in pacemaker dominance and synchronization), as well as sensitivity to metabolic state and oxygen microenvironment.[39−42] Substrate mechanics provide an additional independent axis of variability, as cardiomyocyte structure and contractile dynamics can shift with effective stiffness and cell−substrate coupling.[43,44] Disentangling material-driven contributions (e.g., residual inhibitor species, stiffness evolution, or altered transport properties) from these culture- and device-dependent effects would require a dedicated longitudinal study with orthogonal viability/toxicity readouts and direct oxygen sensing or controlled oxygenation−beyond the scope of this manuscript.

From a practical perspective, maintaining hiPSC-CM monolayers that reliably attach, remain viable, and generate robust contractile activity on microscale compliant structures is itself a nontrivial challenge, and performance is often dominated by biological variability and culture handling rather than by a single materials parameter. In this context, the robust early beating and functional readout achieved on photopatterned devices represents a meaningful validation of compatibility and utility for biologically demanding applications, while controlled long-duration studies remain an important direction for future work.

3.5. Implications for Microfabrication and Biomedical Device Design

The device-level demonstrations illustrate how photopatterned PDMS complements, rather than replaces, established silicone processing approaches. For microfluidic devices, direct photopatterning eliminates the need for molds, enables rapid design iteration, and supports sub-100 μm features using standard laboratory equipment (Figure 4). This capability is particularly useful for prototyping workflows where design flexibility and turnaround time are prioritized.

For cardiac microphysiological systems (MPS), the motivation is fundamentally practical: scalable, human-relevant platforms are needed to evaluate drug efficacy and cardiotoxicity in vitro, and MPS/organ-on-chip approaches have emerged to address gaps in conventional models.[45] Within this landscape, muscular thin-film (MTF) cantilever architectures are attractive because they enable direct, real-time quantification of contractile behavior in compact, potentially parallelized formats.[46] However, many existing implementations rely on stiff photoresists (e.g., SU-8) for structural definition or on thick PDMS slabs for mechanical support, which can complicate quantitative mechanical readout and limit scalable integration.[32,47] In contrast, our photopatterning approach enables thin, mechanically tunable silicone structures to be defined lithographically in commercially available formulations, facilitating integration with embedded strain sensors and fragile cardiomyocyte monolayers in a device geometry that is difficult to achieve with mold-based PDMS processing alone.

In addition to single-layer structures, this approach is compatible in principle with multilayer microfluidic architectures that rely on thin elastomeric membranes (e.g., pneumatic valves and pumps). Classic multilayer soft-lithography and microfluidic large-scale integration (mLSI) use PDMS membrane layers with thicknesses on the order of tens of micrometers (or below) to form deformable elements and dense valve networks.[48] The film thickness regime demonstrated here (2.5−15 μm) overlaps the membrane scale relevant to these architectures, suggesting a practical path to multilayer devices via sequential layer fabrication and bonding/transfer. At the same time, a full valve-array or pumping demonstration would require dedicated optimization of interlayer alignment, bonding yield after solvent development/extraction, and cumulative exposure/optical-transport effects in multiphase formulations; we therefore limit this manuscript to the demonstrated single-

https://doi.org/10.1021/acsapm.5c04718
ACS Appl. Polym. Mater. XXXX, XXX, XXX−XXX

layer microfluidic device and highlight multilayer membrane devices as a natural direction for future work.[48]

More broadly, these results suggest that photopatterned PDMS is most enabling in applications where mechanical compliance, biocompatibility, and multilayer integration are critical, and where moderate resolution is sufficient. Because the process relies on commercially available materials and low-dose UV exposure, it is readily integrated into existing microfabrication and bioengineering workflows, supporting both scalability and translational relevance.

3.6. Mechanistic Framework and Open Questions

The experimental results support a photodeactivated inhibition mechanism in which platinum-catalyzed hydrosilylation is modulated through reversible redox chemistry involving $FeCl_3$ and polyether-mediated photochemistry. While direct observation of transient intermediates is experimentally challenging in this multicomponent system, the convergence of cure-time modulation, compositional controls, and spectroscopic signatures permits a physically consistent mechanistic interpretation grounded in established platinum and iron coordination chemistry.

3.6.1. Reversible Redox Control of Platinum-Catalyzed Hydrosilylation. Across all formulations tested, the addition of $FeCl_3$ substantially prolonged solidification time, indicating effective suppression of platinum-catalyzed hydrosilylation. Selective recovery of rapid curing following UV exposure—observed only in the presence of PEO-containing additives—demonstrates that this inhibition is reversible and can be spatially modulated under illumination. A mechanistic framework consistent with these observations is summarized in Scheme 1

Scheme 1. Proposed Photodeactivated Inhibition Mechanism Underlying Patterned PDMS Solidification[a]

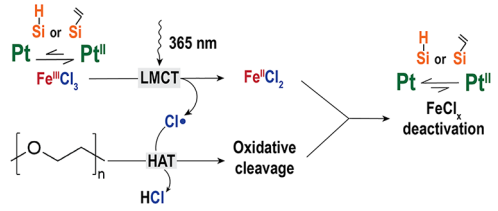

[a]Fe(III) is proposed to inhibit hydrosilylation by oxidizing Pt(0) to higher-valent, catalytically inactive Pt(II)/(IV) species, establishing a reversible redox equilibrium. Under UV illumination, $FeCl_3$ undergoes ligand-to-metal charge transfer (LMCT) in the presence of the PEO−PDMS copolymer, generating chlorine radicals that are quenched by hydrogen atom transfer (HAT), leading to oxidative decomposition of the polyether and depletion of $FeCl_3$. Local depletion of $FeCl_3$ shifts the platinum redox equilibrium toward catalytically active Pt(0), enabling spatially resolved hydrosilylation and accelerated solidification.

A redox-based inhibition mechanism provides thermodynamic and chemical support for these observations. Fe(III) species are capable of oxidizing Pt(0) complexes to higher-valent Pt(II) or Pt(IV) states, which are catalytically inactive toward hydrosilylation. This oxidation step is thermodynamically favorable: $FeCl_3$ exhibits a standard reduction potential of $E(Fe^{3+}/Fe^{2+})$ = +0.8 V vs SCE,[49] while molecular Pt(0) complexes undergo oxidation near $E(Pt^{1+}/Pt^{0}) \approx -0.1$ V vs Fc (corresponding to ≈ +0.3 V vs SCE).[50−52] The resulting potential difference of ∼0.5 V (≈12 kcal mol^{-1}) renders oxidation of Pt(0) by $FeCl_3$ energetically accessible under processing conditions.

Importantly, Pt(II) and Pt(IV) species can be reduced back to catalytically active Pt(0) by vinylsiloxane or hydrosilane monomers, a process well documented in platinum-catalyzed hydrosilylation chemistry.[53,54] This reversible redox behavior underlies the long induction periods observed for platinum precatalysts such as H_2PtCl_6.[55] Within this framework, $FeCl_3$ availability sets the position of a dynamic Pt redox equilibrium: excess $FeCl_3$ maintains platinum in an oxidized, inactive state, while depletion of $FeCl_3$ shifts the system toward Pt(0), enabling rapid cross-linking.

3.6.2. $FeCl_3$−Polyether Photochemistry as the Deinhibition Pathway. The requirement of PEO-containing additives for UV-induced cure acceleration implicates polyether-mediated photochemistry as the route by which $FeCl_3$ is depleted under irradiation. Extensive prior work has shown that $FeCl_3$ undergoes efficient photochemical reduction in the presence of polyethers via ligand-to-metal charge transfer (LMCT) pathways.[56−60] UV excitation generates chlorine radicals, which are rapidly quenched by hydrogen atom transfer from the polyether backbone. The polyether thus acts as a sacrificial reductant, simultaneously consuming $FeCl_3$ and producing oxidized polyether fragments.[61,62]

We propose that the same LMCT-driven pathway operates in the present system. Under UV exposure, $FeCl_3$ is depleted through photoinduced reduction in the presence of PEO−PDMS, thereby removing the oxidizing pressure that maintains platinum in an inactive state. As $FeCl_3$ concentration decreases locally in exposed regions, the Pt redox equilibrium shifts toward catalytically active Pt(0), enabling spatially resolved hydrosilylation and solidification.

3.6.3. Spectroscopic Consistency with Photoinduced $FeCl_3$ Depletion. Spectroscopic measurements provide indirect but consistent support for this model. UV−vis spectra of $FeCl_3$−PEO−PDMS formulations following UV irradiation show disappearance of the characteristic Fe(III)−chloride absorption features between 300−400 nm, indicating substantial conversion of Fe(III) to Fe(II) (Figure 5b).[63,64] This photobleaching correlates directly with accelerated curing in exposed samples, consistent with $FeCl_3$ depletion enabling restoration of platinum catalytic activity.

Complementary FTIR measurements further indicate photoinduced chemical modification of the polyether component. Following UV exposure, new absorption bands emerge near 3400 cm^{-1} and 1630 cm^{-1} (Figure 6e). The former is associated with hydroxyl and hydroperoxide (OOH) functionalities—hallmarks of oxidative degradation—while the latter corresponds to new C−O bond formation, characteristic of polyether oxidation.[61] Prior studies have shown that analogous FTIR features intensify upon oxidative degradation of polyethers and increase with the addition of ethylene glycol, supporting these assignments.[65] No additional spectral features indicative of bulk silicone degradation were observed.

In prior work employing closely related $FeCl_3$−polyether systems to photopattern oxidative polymerization reactions, X-ray photoelectron spectroscopy (XPS) did not reveal persistent shifts in Fe(III)/Fe(II) ratios after illumination.[28] This observation suggests that photoreduction of Fe(III) is reversible, spatially localized, or transient on the time scale of ex situ measurements. Consistent with this interpretation, Fe(III)−chloride absorption bands reappear in UV−vis spectra following dark storage, while macroscopic degradation of the

https://doi.org/10.1021/acsapm.5c04718
ACS Appl. Polym. Mater. XXXX, XXX, XXX−XXX

polyether film—manifested as reduced viscosity and dewetting—persists alongside FTIR signatures of oxidative chain scission.

3.6.4. Experimental Constraints and Outlook. Direct, time-resolved observation of transient iron redox states, platinum oxidation states, or radical intermediates in this system is challenging. The formulation is multiphase, contains volatile or semiliquid components, and undergoes reversible compositional changes under illumination. As a result, conventional ultrahigh-vacuum XPS is poorly suited, because vacuum transfer and pumping can perturb both the chemical speciation and the physical morphology. Cryogenic XPS could, in principle, stabilize short-lived species during measurement and has been applied to reactive coordination complexes and hydrated soft-matter interfaces,[66] but it requires specialized instrumentation beyond the scope of this work.

Electron spin resonance (ESR) spectroscopy with spin trapping could also probe radical intermediates.[67] In practice, however, capturing chlorine- or polyether-derived radicals would require stringent oxygen exclusion and subsecond temporal resolution. Moreover, the reversible, illumination-dependent Fe(III)/Fe(II) interconversion may keep radical concentrations below steady-state detection limits under typical ESR conditions.

We also considered time-resolved FTIR to track functional-group consumption during hydrosilylation. Although the Si−H band near 2100−2168 cm^{-1} is observable, we did not obtain reproducible time-dependent changes in Si−H intensity or in the substantially weaker vinyl bands under the thin-film, multiphase, processing-relevant conditions used here. Quantitative FTIR kinetics in hydrosilylation systems typically relies on careful control of stoichiometry, optical path length/geometry, and an in situ reaction configuration—constraints that would introduce a different experimental regime than our application-driven objective of optimizing solidification contrast in thin films of commercially available silicones.

Despite these constraints, the close agreement among cure-time modulation, formulation dependence, UV−vis photobleaching, FTIR signatures of polyether oxidation, and control experiments provides strong indirect support for a photodeactivated inhibition mechanism mediated by $FeCl_3$ depletion and platinum redox chemistry. Together, these observations outline a coherent physical picture while motivating future operando spectroscopic studies to further resolve transient intermediates.

4. CONCLUSION

In this work, we developed a rapid and accessible method for photopatterning a wide range of commercially available silicone elastomers using an off-the-shelf, photodeactivated hydrosilylation inhibitor. Our approach leverages a $FeCl_3$−PEO emulsion, standard 365 nm UV exposure, and solvent development steps to define features as small as 20 μm with exposure doses as low as 117 mJ cm^{-2}. Unlike many existing methods that require custom catalyst synthesis, oxygen exclusion, or high-energy UV sources, our strategy is compatible with common laboratory equipment and relies exclusively on widely available materials. The same protocol was successfully applied to both clear dielectric gels (Sylgard 184, Sylgard 527) and highly filled elastomers (Ecoflex, Dragon Skin), underscoring its generalizability and scalability.

Compared to prior silicone photopatterning approaches—many of which are limited to 100−200 μm feature sizes and require exposure doses exceeding 7000 mJ cm^{-2} [1,8,10,11,13,14,17,20,68−70]—our method represents a significant advance in both resolution and accessibility. Importantly, the patterned Sylgard-based films retained their optical clarity, local mechanical properties, and biocompatibility, enabling direct application in biological systems. We demonstrated this through two proof-of-concept devices: a microfluidic flow-focusing chip and a cardiac microphysiological system with integrated strain sensors, both fabricated entirely using this photopatterning process. Our approach achieves mechanical performance comparable to benzophenone-based techniques, but with greater tunability across a broader range of silicone formulations. This versatility makes the method particularly well suited for applications where pattern fidelity, biocompatibility, and tailored mechanical properties are critical.

Nonetheless, some limitations remain. The emulsion-based formulation can introduce light-scattering interfaces that may reduce resolution, particularly in heavily filled silicones, and performance is sensitive to emulsion droplet size and dispersion quality. Sidewall angles were found to depend strongly on the mask-to-substrate gap, suggesting that edge fidelity could be improved through tighter control of exposure geometry, projection lithography, and/or the use of refractive index-matching media. While local mechanical properties were preserved in transparent elastomers, our mechanical characterization was limited in scope and future work should include more comprehensive mechanical testing relevant to device operation (e.g., viscoelasticity, fatigue/cyclic loading, and property drift over time). In addition, long-term material stability and degradation pathways remain to be established, including potential leaching of residual inhibitor/byproducts, changes under prolonged aqueous culture or sterilization conditions, and the durability of patterned features during extended use. Finally, although the patterned devices supported functional hIPSC-derived cardiomyocyte monolayers under the conditions tested, longer-term cell viability and biocompatibility should be assessed quantitatively (and across additional cell types) to fully define safe operating windows for biointerfaces. Future work could also benefit from more comprehensive multivariate optimization of formulation and processing parameters, as well as operando mechanistic studies (e.g., time-resolved spectroscopy or cryogenic/oxygen-excluded measurements) to directly probe transient redox and radical intermediates that are difficult to capture under processing-relevant, multiphase thin-film conditions.

Despite these challenges, this work introduces a simple, tunable, and broadly applicable method for direct photopatterning of silicone elastomers, addressing a longstanding need for high-resolution patterning with minimal barriers to adoption. Because it leverages only off-the-shelf materials and standard 365 nm tools, the method is readily translatable into both academic and industrial settings, enabling rapid iteration in device prototyping and large-scale fabrication. We anticipate that this technique will accelerate the development of soft robotics, microfluidics, and biomedical platforms by lowering the barrier to entry for precise silicone microfabrication.

In sum, this work establishes $FeCl_3$−PEO as a broadly accessible photodeactivated inhibitor platform for silicone patterning—uniquely combining commercial availability, high-resolution performance, and scalability—and paves the way for widespread integration into advanced microfabrication and bioengineering applications.

https://doi.org/10.1021/acsapm.5c04718
ACS Appl. Polym. Mater. XXXX, XXX, XXX−XXX

■ ASSOCIATED CONTENT

Supporting Information

The Supporting Information is available free of charge at https://pubs.acs.org/doi/10.1021/acsapm.5c04718.

Representative video of a photopatterned silicone cantilever with cultured hIPSC-derived cardiomyocytes showing cyclic deflection during spontaneous contractions (real-time) (MP4)

Detailed materials lists; substrate cleaning procedures; preparation and optimization of the $FeCl_3$−PEO−PDMS photodeactivated inhibitor; preparation of photopatternable commercial silicones (Sylgard 184, Sylgard 527, Dragon Skin 10 Medium, Ecoflex 00−30) and custom silicone formulations; film preparation, UV exposure, curing, and development protocols; synthesis of Ag nanowires and Au-coated Ag nanowires; shadow mask fabrication; detailed characterization methods (UV−vis spectroscopy, optical transparency, nanoindentation, water-assisted tensile testing, profilometry, FTIR, and biocompatibility assays); device fabrication protocols for microfluidic devices and cardiac microphysiological devices with integrated sensors (including cardiomyocyte culture and data acquisition/analysis); comparison of key performance metrics between our photopatternable silicone system and representative prior systems reported in the literature; characteristics of the photopatterning process using Sylgard 184; film thickness of Sylgard 184 mixed the 0.1 mL/g of the photodeactivated inhibitor; stress vs strain data obtained through water-assisted tensile testing; comparison of full-thickness silicone patterning techniques; and additional process optimization notes and references (PDF)

■ AUTHOR INFORMATION

Corresponding Author

Darren J. Lipomi − *Aiiso Yufeng Li Family Department of Chemical and Nano Engineering, University of California, San Diego, La Jolla, California 92093-0448, United States;* Present Address: Department of Chemical and Sustainability Engineering, University of Rochester, 500 Joseph C. Wilson Blvd. Rochester, New York 14627, United States; orcid.org/0000-0002-5808-7765; Email: darren.lipomi@rochester.edu

Authors

Samuel J. Edmunds − *Department of Electrical Engineering, University of California, San Diego, La Jolla, California 92093-0448, United States;* Present Address: HRL Laboratories, 3011 Malibu Canyon Road, Malibu, California 90265−4797, United States

Noel Sebastien D. Mallari − *Aiiso Yufeng Li Family Department of Chemical and Nano Engineering, University of California, San Diego, La Jolla, California 92093-0448, United States*

Marc N. Levy − *Aiiso Yufeng Li Family Department of Chemical and Nano Engineering, University of California, San Diego, La Jolla, California 92093-0448, United States*

Qinyu Liang − *Department of Chemistry and Biochemistry, University of California, San Diego, La Jolla, California 92093-0309, United States*

Anum Tahir − *Aiiso Yufeng Li Family Department of Chemical and Nano Engineering, University of California, San Diego, La Jolla, California 92093-0448, United States*

Dhivya Pushpa Meganathan − *Aiiso Yufeng Li Family Department of Chemical and Nano Engineering, University of California, San Diego, La Jolla, California 92093-0448, United States*

Lisa Tang − *Aiiso Yufeng Li Family Department of Chemical and Nano Engineering, University of California, San Diego, La Jolla, California 92093-0448, United States;* orcid.org/0000-0001-5312-673X

Leah Sadr − *Aiiso Yufeng Li Family Department of Chemical and Nano Engineering, University of California, San Diego, La Jolla, California 92093-0448, United States*

Jacqueline Lampert − *Aiiso Yufeng Li Family Department of Chemical and Nano Engineering, University of California, San Diego, La Jolla, California 92093-0448, United States*

Wade Shipley − *Aiiso Yufeng Li Family Department of Chemical and Nano Engineering, University of California, San Diego, La Jolla, California 92093-0448, United States*

Hannah E. Fishman − *Aiiso Yufeng Li Family Department of Chemical and Nano Engineering, University of California, San Diego, La Jolla, California 92093-0448, United States*

Rafael A. Montalvo − *Aiiso Yufeng Li Family Department of Chemical and Nano Engineering, University of California, San Diego, La Jolla, California 92093-0448, United States*

Tarek Rafeedi − *Aiiso Yufeng Li Family Department of Chemical and Nano Engineering, University of California, San Diego, La Jolla, California 92093-0448, United States*

Abdulhameed Abdal − *Aiiso Yufeng Li Family Department of Chemical and Nano Engineering, University of California, San Diego, La Jolla, California 92093-0448, United States; Department of Biomedical and Instruments Engineering, Abdullah Al Salem University, 12037 Kuwait City, Kuwait;* orcid.org/0000-0002-7397-5920

Tse Nga Ng − *Department of Electrical Engineering, University of California, San Diego, La Jolla, California 92093-0448, United States; Program in Materials Science and Engineering, University of California, San Diego, La Jolla, California 92093, United States;* orcid.org/0000-0001-6967-559X

Jinhye Bae − *Aiiso Yufeng Li Family Department of Chemical and Nano Engineering, University of California, San Diego, La Jolla, California 92093-0448, United States;* orcid.org/0000-0002-2536-069X

Andrea R. Tao − *Aiiso Yufeng Li Family Department of Chemical and Nano Engineering, University of California, San Diego, La Jolla, California 92093-0448, United States;* orcid.org/0000-0003-1857-8743

Nathan A. Romero − *Department of Chemistry and Biochemistry, University of California, San Diego, La Jolla, California 92093-0309, United States;* orcid.org/0000-0001-8127-4617

Zeinab Jahed − *Aiiso Yufeng Li Family Department of Chemical and Nano Engineering, University of California, San Diego, La Jolla, California 92093-0448, United States;* orcid.org/0000-0002-0139-3219

Complete contact information is available at: https://pubs.acs.org/10.1021/acsapm.5c04718

Notes

The authors declare no competing financial interest.

https://doi.org/10.1021/acsapm.5c04718
ACS Appl. Polym. Mater. XXXX, XXX, XXX−XXX

■ ACKNOWLEDGMENTS

This research was supported primarily by the National Institutes of Health, award number 1R21GM137151. A.T. and D.J.L. acknowledge support from the NSF Materials Research Science and Engineering (MRSEC) at UC San Diego funded under grant DMR-2011924. Z.J. acknowledges support from the Air Force Office of Scientific Research under grant number FA9550-23-1-0090. J.B. acknowledges support from the National Research Foundation of Korea (NRF) funded by the Ministry of Science and ICT (MSIT), RS-2025-00557115. N.R. acknowledges support from the National Science Foundation grant number award CHE-2305056. A.A. acknowledges the support of the Kuwait Foundation for the Advancement of Sciences (KFAS).

■ REFERENCES

(1) Kim, S.; Kang, J.; Lee, I.; Jang, J.; Park, C. B.; Lee, W.; Bae, B.-S. An intrinsically stretchable multi-biochemical sensor for sweat analysis using photo-patternable ecoflex. *npj Flexible Electron.* **2023**, *7*, No. 33.
(2) Chen, S.; Qiao, Z.; Niu, Y.; Yeo, J. C.; Liu, Y.; Qi, J.; Fan, S.; Liu, X.; Lee, J. Y.; Lim, C. T. Wearable flexible microfluidic sensing technologies. *Nat. Rev. Bioeng.* **2023**, *1*, 950−971.
(3) Borenstein, J. T.; Cummins, G.; Dutta, A.; Hamad, E.; Pycraft Hughes, M.; Jiang, X.; Lee, H. H.; Fong Lei, K.; Tang, X. S.; Zheng, Y.; Chen, J. Bionanotechnology and bioMEMS (BNM): state-of-the-art applications, opportunities, and challenges. *Lab Chip* **2023**, *23*, 4928−4949.
(4) Xia, Y.; Whitesides, G. M. Soft Lithography. *Angew. Chem., Int. Ed.* **1998**, *37*, 550−575.
(5) Wu, C.; Xu, J.; Zhang, T.; Xin, G.; Li, M.; Rong, Y.; Zhang, G.; Huang, Y. Precision cutting of PDMS film with UV-nanosecond laser based on heat generation-diffusion regulation. *Optics Laser Technol.* **2022**, *145*, No. 107462.
(6) Helgason, R.; Fathy, J.; Lai, Y. The effect of laser cutting on the Young's modulus of Polydimethylsiloxane. *J. Micromanuf.* **2023**, *6*, 60−65.
(7) Jackman, R. J.; Duffy, D. C.; Cherniavskaya, O.; Whitesides, G. M. Using Elastomeric Membranes as Dry Resists and for Dry Lift-Off. *Langmuir* **1999**, *15*, 2973−2984.
(8) Harkness, B. R.; Gardner, G. B.; Alger, J. S.; Cummings, M. R.; Princing, J.; Lee, Y.; Meynen, H.; Gonzales, M.; Vandevelde, B.; Bulcke, M. V.; Winters, C.; Beyne, E. In *Photopatternable Silicone Compositions for Electronic Packaging Applications*, Advances in Resist Technology and Processing XXI; SPIE, 2004; pp 517−524.
(9) Brook, M. A. Functional silicone oils and elastomers: new routes lead to new properties. *Chem. Commun.* **2023**, *59*, 12813−12829.
(10) Gao, S.; Tung, W.-T.; Wong, D. S.-H.; Bian, L.; Zhang, A. P. Direct optical micropatterning of poly(dimethylsiloxane) for microfluidic devices. *J. Micromech. Microeng.* **2018**, *28*, No. 095011.
(11) Müller, U.; Kunze, A.; Herzig, C.; Weis, J. Photocrosslinking of Silicones. Part 13. Photoinduced Thiol-Ene Crosslinking of Modified Silicones. *J. Macromol. Sci., Part A* **1996**, *33*, 439−457.
(12) Wu, Y.; Liu, J.; Jiao, X.; Cheng, F.; Lai, G.; Yang, X. UV-Cured Transparent Flexible Silicone Materials with High Tensile Strength. *ACS Omega* **2020**, *5*, 6199−6206.
(13) Xiang, H.; Wang, X.; Ou, Z.; Lin, G.; Yin, J.; Liu, Z.; Zhang, L.; Liu, X. UV-curable, 3D printable and biocompatible silicone elastomers. *Prog. Org. Coat.* **2019**, *137*, No. 105372.
(14) Nguyen, K. D. Q.; Megone, W. V.; Kong, D.; Gautrot, J. E. Ultrafast diffusion-controlled thiol—ene based crosslinking of silicone elastomers with tailored mechanical properties for biomedical applications. *Polym. Chem.* **2016**, *7*, 5281−5293.
(15) Jiang, B.; Shi, X.; Zhang, T.; Huang, Y. Recent advances in UV/thermal curing silicone polymers. *Chem. Eng. J.* **2022**, *435*, No. 134843.
(16) Lukin, R. Y.; Kuchkaev, A. M.; Sukhov, A. V.; Bekmukhamedov, G. E.; Yakhvarov, D. G. Platinum-Catalyzed Hydrosilylation in Polymer Chemistry. *Polymers* **2020**, *12*, No. 2174.
(17) Bhagat, S.; Jothimuthu, A. A.; Papautsky, P. Photodefinable polydimethylsiloxane (PDMS) for rapid lab-on-a-chip prototyping. *Lab Chip* **2007**, *7*, 1192−1197.
(18) Stricher, A.; Rinaldi, R. G.; Machado, G.; Chagnon, G.; Favier, D.; Chazeau, L.; Ganachaud, F. Light-Induced Bulk Architecturation of PDMS Membranes. *Macromol. Mater. Eng.* **2016**, *301*, 1151−1157.
(19) Stricher, A.; Rinaldi, R. G.; Chazeau, L.; Ganachaud, F. Photopatterning of PDMS Films: Challenging the Reaction between Benzophenone and Silicone Functional Groups. *Materials* **2021**, *14*, No. 2027.
(20) Jothimuthu, P.; Carroll, A.; Bhagat, A. A. S.; Lin, G.; Mark, J. E.; Papautsky, I. Photodefinable PDMS thin films for microfabrication applications. *J. Micromech. Microeng.* **2009**, *19*, No. 045024.
(21) Radchenko, A. V.; Ganachaud, F. Photocatalyzed Hydrosilylation in Silicone Chemistry. *Ind. Eng. Chem. Res.* **2022**, *61*, 7679−7698.
(22) Lancaster, H. G.; Goodall, J. C.; Douglas, S. P.; Ashfield, L. J.; Duckett, S. B.; Perutz, R. N.; Weller, A. S. Platinum(II) Phenylpyridyl Schiff Base Complexes as Latent, Photoactivated, Alkene Hydrosilylation Catalysts. *ACS Catal.* **2024**, *14*, 7492−7505.
(23) Sangermano, M.; Marchi, S.; Ligorio, D.; Meier, P.; Kornmann, X. UV-Induced Frontal Polymerization of a Pt-Catalyzed Hydrosilation Reaction. *Macromol. Chem. Phys.* **2013**, *214*, 943−947.
(24) Mayer, T.; Burget, D.; Mignani, G.; Fouassier, J. P. Photohydrosilylation reaction of silicone polymers. Platinum-based photocatalysts: Trimethyl(SS-dicarbonyl) platinum IV complexes. *J. Polym. Sci., Part A: Polym. Chem.* **1996**, *34*, 3141−3146.
(25) Xi, L.; Liu, Z.; Su, J.; Bei, Y.; Xiang, H.; Liu, X. UV-activated hydrosilylation of (Me-Cp)Pt(Me)3: Enhanced photocatalytic activity, polymerization kinetics, and photolithography. *J. Appl. Polym. Sci.* **2019**, *136*, No. 48251.
(26) Marchi, S.; Sangermano, M.; Meier, P.; Kornmann, X. Visible light-activated hydrosilation reaction. *J. Photochem. Photobiol., A* **2015**, *303*−*304*, 86−90.
(27) Marchi, S.; Sangermano, M.; Meier, P.; Kornmann, X. A Comparison of the Reactivity of Two Platinum Catalysts for Silicone Polymer Cross-Linking by UV-Activated Hydrosilation Reaction. *Macromol. React. Eng.* **2015**, *9*, 360−365.
(28) Edmunds, S. J.; Urbina, A. D.; Fishman, H. E.; Qie, Y.; Montalvo, R. A.; Mallari, N. S. D.; Levy, M. N.; Blau, R.; Abdal, A.; Armani, A. M.; Ng, T. N.; Romero, N. A.; Lipomi, D. J. Photography-Inspired Patterned Vapor Phase Polymerization of Conductive PEDOT on Rigid and Stretchable Substrates. *ACS Mater. Lett.* **2024**, *6*, 2738−2747.
(29) Sarikhani, E.; Patel, V.; Li, Z.; et al. Engineered Nanotopographies Induce Transient Openings in the Nuclear Membrane. *Adv. Funct. Mater.* **2025**, *35*, No. 2410035.
(30) White, C. C.; VanLandingham, M. R.; Drzal, P. L.; Chang, N.-K.; Chang, S.-H. Viscoelastic characterization of polymers using instrumented indentation. II. Dynamic testing. *J. Polym. Sci., Part B: Polym. Phys.* **2005**, *43*, 1812−1824.
(31) Lin, I.-K.; Liao, Y.-M.; Liu, Y.; Ou, K.-S.; Chen, K.-S.; Zhang, X. Viscoelastic mechanical behavior of soft microcantilever-based force sensors. *Appl. Phys. Lett.* **2008**, *93*, No. 251907.
(32) Kim, D. S.; Choi, Y. W.; Shanmugasundaram, A.; Jeong, Y. J.; Park, J.; Oyunbaatar, N. E.; Kim, E. S.; Choi, M.; Lee, D. W. Highly durable crack sensor integrated with silicone rubber cantilever for measuring cardiac contractility. *Nat. Commun.* **2020**, *11*, No. 535.
(33) Weidauer, M.; Heyder, B.; Woelki, D.; Tschiersch, M.; Köhler-Krützfeldt, A.; Enthaler, S. Iron-catalyzed depolymerizations of end-of-life silicones with fatty alcohols. *Resour.-Effic.Technol.* **2015**, *1*, 73−79.
(34) Enthaler, S.; Kretschmer, R. Low-Temperature Depolymerization of Polysiloxanes with Iron Catalysis. *ChemSusChem* **2014**, *7*, 2030−2036.
(35) Enthaler, S. Iron-catalyzed depolymerization of polysiloxanes to produce dichlorodimethylsilane, diacetoxydimethylsilane, or dimethoxydimethylsilane. *J. Appl. Polym. Sci.* **2015**, *132*, 41287.
(36) Rupasinghe, B.; Furgal, J. C. Degradation of silicone-based materials as a driving force for recyclability. *Polym. Int.* **2022**, *71*, 521−531.

https://doi.org/10.1021/acsapm.5c04718
ACS Appl. Polym. Mater. XXXX, XXX, XXX−XXX

(37) Carter, S.-S. D.; Atif, A.-R.; Kadekar, S.; Lanekoff, I.; Engqvist, H.; Varghese, O. P.; Tenje, M.; Mestres, G. PDMS leaching and its implications for on-chip studies focusing on bone regeneration applications. *Organs-on-a-Chip* **2020**, *2*, No. 100004.
(38) Millet, L. J.; Stewart, M. E.; Sweedler, J. V.; Nuzzo, R. G.; Gillette, M. U. Microfluidic devices for culturing primary mammalian neurons at low densities. *Lab Chip* **2007**, *7*, 987−994.
(39) Guerrelli, D.; Pressman, J.; Salameh, S.; Posnack, N. hiPSC-CM electrophysiology: impact of temporal changes and study parameters on experimental reproducibility. *A. J. Physiol.-Heart Circ. Physiol.* **2024**, *327*, H12−H27.
(40) Seibertz, F.; Sutanto, H.; Dülk, R.; et al. Electrophysiological and calcium-handling development during long-term culture of human-induced pluripotent stem cell-derived cardiomyocytes. *Basic Res. Cardiol.* **2023**, *118*, No. 14.
(41) Rivera, K. R.; Yokus, M. A.; Erb, P. D.; Pozdin, V. A.; Daniele, M. Measuring and regulating oxygen levels in microphysiological systems: Design, material, and sensor considerations. *Analyst* **2019**, *144*, 3190−3215.
(42) Rexius-Hall, M. L.; Khalil, N. N.; Escopete, S. S.; Li, X.; Hu, J.; Yuan, H.; Parker, S. J.; McCain, M. L. A myocardial infarct border-zone-on-a-chip demonstrates distinct regulation of cardiac tissue function by an oxygen gradient. *Sci. Adv.* **2022**, *8*, No. eabn7097.
(43) Engler, A. J.; Carag-Krieger, C.; Johnson, C. P.; Raab, M.; Tang, H.-Y.; Speicher, D. W.; Sanger, J. W.; Sanger, J. M.; Discher, D. E. Embryonic cardiomyocytes beat best on a matrix with heart-like elasticity: scar-like rigidity inhibits beating. *J. Cell Sci.* **2008**, *121*, 3794−3802.
(44) Körner, A.; Mosqueira, M.; Hecker, M.; Ullrich, N. D. Substrate Stiffness Influences Structural and Functional Remodeling in Induced Pluripotent Stem Cell-Derived Cardiomyocytes. *Front. Physiol.* **2021**, *12*, No. 710619.
(45) Vunjak-Novakovic, G.; Ronaldson-Bouchard, K.; Radisic, M. Organs-on-a-chip models for biological research. *Cell* **2021**, *184*, 4597−4611.
(46) del Álamo, J. C.; Lemons, D.; Serrano, R.; Savchenko, A.; Cerignoli, F.; Bodmer, R.; Mercola, M. High throughput physiological screening of iPSC-derived cardiomyocytes for drug development. *Biochim. Biophys. Acta, Mol. Cell Res.* **2016**, *1863*, 1717−1727.
(47) Dai, Y.; Oyunbaatar, N. E.; Lee, B. K.; Kim, E. S.; Lee, D. W. Spiral-shaped SU-8 cantilevers for monitoring mechanical response of cardiomyocytes treated with cardiac drugs. *Sens. Actuators, B* **2018**, *255*, 3391−3399.
(48) Melin, J.; Quake, S. R. Microfluidic Large-Scale Integration: The Evolution of Design Rules for Biological Automation. *Annu. Rev. Biophys. Biomol. Struct.* **2007**, *36*, 213−231.
(49) Wu, W.; He, X.; Fu, Z.; Liu, Y.; Wang, Y.; Gong, X.; Deng, X.; Wu, H.; Zou, Y.; Yu, N.; Yin, D. Metal chlorides-catalyzed selective oxidation of cyclohexane by molecular oxygen under visible light irradiation. *J. Catal.* **2012**, *286*, 6−12.
(50) Troadec, T.; Tan, S.-y.; Wedge, C. J.; Rourke, J. P.; Unwin, P. R.; Chaplin, A. B. One-Electron Oxidation of [M(PtBu3)2] (M = Pd, Pt): Isolation of Monomeric [Pd(PtBu3)2]+ and Redox-Promoted CH Bond Cyclometalation. *Angew. Chem., Int. Ed.* **2016**, *55*, 3754−3757.
(51) MacInnis, M. C.; DeMott, J. C.; Zolnhofer, E. M.; Zhou, J.; Meyer, K.; Hughes, R. P.; Ozerov, O. V. Cationic Two-Coordinate Complexes of Pd(I) and Pt(I) Have Longer Metal-Ligand Bonds Than Their Neutral Counterparts. *Chem* **2016**, *1*, 902−920.
(52) Pavlishchuk, V. V.; Addison, A. W. Conversion constants for redox potentials measured versus different reference electrodes in acetonitrile solutions at 25°C. *Inorg. Chim. Acta* **2000**, *298*, 97−102.
(53) Hitchcock, P. B.; Lappert, M. F.; Warhurst, N. J. W. Synthesis and Structure of a rac-Tris(divinyldisiloxane) diplatinum(0) Complex and its Reaction with Maleic Anhydride. *Angew. Chem., Int. Ed.* **1991**, *30*, 438−440.
(54) de Vekki, D. A.; Spevak, V. N.; Kuchaev, E. A.; Skvortsov, N. K. Hydrosilylation of Siloxanes in the Presence of Pt(II) and Pt(IV) Complexes. *Russ. J. Gen. Chem.* **2005**, *75*, 1757−1762.
(55) Stein, J.; Lewis, L. N.; Gao, Y.; Scott, R. A. In Situ Determination of the Active Catalyst in Hydrosilylation Reactions Using Highly Reactive Pt(0) Catalyst Precursors. *J. Am. Chem. Soc.* **1999**, *121*, 3693−3703.
(56) Gonzalez, M. I.; Gygi, D.; Qin, Y.; Zhu, Q.; Johnson, E. J.; Chen, Y.-S.; Nocera, D. G. Taming the Chlorine Radical: Enforcing Steric Control over Chlorine-Radical-Mediated C−H Activation. *J. Am. Chem. Soc.* **2022**, *144*, 1464−1472.
(57) Lim, M.; Chiang, K.; Amal, R. Photochemical synthesis of chlorine gas from iron(III) and chloride solution. *J. Photochem. Photobiol., A* **2006**, *183*, 126−132.
(58) Qi, Y.; Luo, S.; Li, W.; Li, S.; Chen, Z.; Tian, B.; Liu, S. Visible-light-initiated air-oxygenation of 5-hydroxymethylfurfural to maleic acid by iron(III) chloride. *Chem. Eng. J.* **2024**, *487*, No. 150580.
(59) Rogolino, A.; Filho, J. B. G.; Fritsch, L.; Ardisson, J. D.; da Silva, M. A. R.; Atta Diab, G. A.; Silva, I. F.; Moraes, C. A. F.; Forim, M. R.; Bauer, M.; Kühne, T. D.; Antonietti, M.; Teixeira, I. F. Direct Synthesis of Acetone by Aerobic Propane Oxidation Promoted by Photoactive Iron(III) Chloride under Mild Conditions. *ACS Catal.* **2023**, *13*, 8662−8669.
(60) Zhang, Z.; Zhang, G.; Xiong, N.; Xue, T.; Zhang, J.; Bai, L.; Guo, Q.; Zeng, R. Oxidative -C−C Bond Cleavage of 2° and 3° Alcohols to Aromatic Acids with O2 at Room Temperature via Iron Photocatalysis. *Org. Lett.* **2021**, *23*, 2915−2920.
(61) Rabek, J. F.; Lindén, L.; Kaczmarek, H.; Qu, B. J.; Shi, W. F. Photodegradation of poly(ethylene oxide) and its coordination complexes with iron(III)chloride. *Polym. Degrad. Stab.* **1992**, *37*, 33−40.
(62) Rabek, J. F.; Lucki, J.; Qu, B. J.; Shi, W. F. Coordination complexes between iron(III) chloride and polyether, polyester, and poly(ether ester). *Macromolecules* **1991**, *24*, 836−843.
(63) Jin, Y.; Zhang, Q.; Wang, L.; Wang, X.; Meng, C.; Duan, C. Convenient C(sp 3)−H bond functionalisation of light alkanes and other compounds by iron photocatalysis. *Green Chem.* **2021**, *23*, 6984−6989.
(64) Wu, Q.; Hu, P. Photoinduced C−O Bond Formation through CC Bond Cleavage of Alcohols by Suppressing Alcohol Oxidation. *Adv. Synth. Catal.* **2024**, *366*, 1595−1605.
(65) Caccamo, M. T.; Magazù, S. Ethylene Glycol − Polyethylene Glycol (EG-PEG) Mixtures: Infrared Spectra Wavelet Cross-Correlation Analysis. *Appl. Spectrosc.* **2017**, *71*, 401−409.
(66) Shchukarev, A.; Ramstedt, M. Cryo-XPS: probing intact interfaces in nature and life. *Surf. Interface Anal.* **2017**, *49*, 349−356.
(67) Yamada, B.; Westmoreland, D. G.; Kobatake, S.; Konosu, O. ESR spectroscopic studies of radical polymerization. *Prog. Polym. Sci.* **1999**, *24*, 565−630.
(68) Zhang, C.; Wang, W.; He, W.; Xi, N.; Wang, Y.; Liu, L. Dynamic Model for Characterizing Contractile Behaviors and Mechanical Properties of a Cardiomyocyte. *Biophys. J.* **2018**, *114*, 188−200.
(69) Holländer, J.; Hakala, R.; Suominen, J.; Moritz, N.; Yliruusi, J.; Sandler, N. 3D printed UV light cured polydimethylsiloxane devices for drug delivery. *Int. J. Pharm.* **2018**, *544*, 433−442.
(70) Putzien, S.; Louis, E.; Nuyken, O.; Crivello, J. V.; Kühn, F. E. UV curing of epoxy functional hybrid silicones. *J. Appl. Polym. Sci.* **2012**, *126*, 1188−1197.

https://doi.org/10.1021/acsapm.5c04718
ACS Appl. Polym. Mater. XXXX, XXX, XXX−XXX